Mechanisms of Unrest and Eruption at Persistently Restless Volcanoes: Insights From the 2015 Eruption of Telica Volcano, Nicaragua

N.B. When citing this work, cite the original published paper.

(article starts on next page)

Mechanisms of Unrest and Eruption at Persistently Restless Volcanoes: Insights From the 2015 Eruption of Telica Volcano, Nicaragua

Diana C. Roman[1] , Peter C. LaFemina[2] , Rebecca Bussard[2], Kirsten Stephens[2] , Christelle Wauthier[2] , Machel Higgins[2], Maureen Feineman[2], Santiago Arellano[3] , J. Maarten de Moor[4], Geoffroy Avard[4] , Maria Martinez Cruz[4] , Mike Burton[5] , Matthew Varnam[5] , Armando Saballos[6], Martha Ibarra[6], Wilfried Strauch[6], and Virginia Tenorio[6]

[1]Department of Terrestrial Magnetism, Carnegie Institution for Science, Washington, DC, USA, [2]Department of Geosciences, The Pennsylvania State University, University Park, PA, USA, [3]Department of Space, Earth and Environment, Chalmers University of Technology, Gothenburg, Sweden, [4]Observatorio Vulcanológico y Sismológico de Costa Rica, Universidad Nacional de Costa Rica, Heredia, Costa Rica, [5]School of Earth and Environmental Sciences, The University of Manchester, Manchester, UK, [6]Instituto Nicaragüense de Estudios Territoriales, Managua, Nicaragua

Abstract Many of Earth's volcanoes experience well-defined states of "quiescence" and "unrest," with unrest occasionally culminating in eruption. Some volcanoes, however, experience an unusually protracted (i.e., decades-long) period of noneruptive unrest and are thus categorized as "persistently restless volcanoes" (PRVs). The processes that drive persistently restless volcanism are poorly understood, as our knowledge of PRVs is currently based on a small number of case studies. Here we examine multidisciplinary observations of the 2015 eruptive episode at Telica Volcano, Nicaragua, in the context of its long-term behavior. We suggest that the latter phases of the 2015 eruption were ultimately driven by destabilization of its shallow magma reservoir. Based on previous geodetic-seismic studies of Telica (Geirsson et al., 2014, https://doi.org/10.1016/j.jvolgeores.2013.11.009; Rodgers et al., 2013, https://doi.org/10.1016/j.jvolgeores.2013.08.010 and 2015, https://doi.org/10.1016/j.jvolgeores.2014.11.012) and on multiparameter observations at Telica over a 7-year period, we propose that three distinct states of unrest occur at Telica over decadal timescales: a stable open state involving steady conduit convection and two distinct "unstable" states that may lead to eruptions. In the "weak sealing" state, phreatic explosions result from steady conduit convection underlying a weak seal. In the "destabilized" state, destabilization of the top of the convecting magma in the conduit leads to rapid accumulation of high pressures leading to strong/impulsive phreatomagmatic explosions. Our observations and interpretations suggest that continuous seismic, ground-based deformation, gas emission, and thermal monitoring and interpretation of these data within a paradigm of sustained conduit convection modulated by episodes of sealing and destabilization of shallow magma reservoirs may allow robust forecasting of eruption potential, energy, and duration at Telica and similar PRVs worldwide.

1. Introduction

Many of Earth's volcanoes appear to experience well-defined states of "quiescence" and "unrest" (characterizable by levels of seismic activity, deformation, and degassing), with unrest occasionally culminating in eruption. The transition from quiescence to unrest, which is generally observable with instrumental monitoring, typically occurs over weeks to months (e.g., Johnson et al., 2010; Nakada et al., 1999; Wolfe & Hoblitt, 1996) and provides an indication that an eruption may be imminent. The transition to unrest and, in some cases, eruption at these volcanoes is generally understood to result from a discrete episode of upward migration of magma and/or volatiles from a deeper region in the volcano's plumbing system (Cashman et al., 2017). Following eruptions, the return to quiescence again occurs over weeks to months (e.g., Mori et al., 1996; Power et al., 2013).

Some volcanoes, however, experience an unusually protracted (i.e., years to decades) period of noneruptive unrest and are thus categorized as "persistently restless volcanoes" (PRVs). PRVs, examples of which include Shishaldin Volcano, Alaska; Tatun Volcano, Taiwan; and Turrialba Volcano, Costa Rica, have long-term

elevated seismic and/or degassing activity, punctuated by occasional phreatic, phreatomagmatic, or magmatic eruptions. The processes that drive persistently restless volcanism are poorly understood, as our knowledge of PRVs is currently based on a small number of case studies (e.g., Kumagai et al., 2014; Park et al., 2019; Petersen et al., 2006) using disparate geophysical and geochemical observational techniques. Stix (2018) proposed that activity at PRVs ("volcanoes with slow unrest" in his study) involves slow, fitful rise of magma which may never reach the surface, an absence of a well-defined reservoir with magma storage and transport instead occurring in a complex of dikes and sills, and a relatively open connection between the shallow magmatic system and the surface. While this model is consistent with observations of several recent magmatic eruptions (e.g., Turrialba Volcano, Costa Rica and Soufriere Hills Volcano, Montserrat), it does not fully explain observations at PRVs characterized by dominantly phreatic eruptions with little or no evidence of shallow magma emplacement and thus motivates detailed multiparameter and comparative analyses of long-term activity at these PRVs to further develop a general model for both long- and short-term unrest and eruption in these systems.

We operated a broadband seismic and continuous Global Positioning System (cGPS) network at the persistently restless Telica Volcano, Nicaragua, from November 2009 to November 2016 (the Telica Seismic and Deformation [TESAND] network). During this 7-year period, data from the TESAND network were complemented by regular visual observations of the crater and of eruptive activity and episodic temperature and gas measurements. During the TESAND deployment, Telica experienced two VEI 2 eruptions, one in 2011 and one in 2015. Geirsson et al. (2014) and Rodgers et al. (2015) discussed and synthesized observations before and during the 2011 eruption. Key aspects of the 2011 eruption were (1) eruption of nonjuvenile, hydrothermally altered ash during phreatic explosions; (2) a lack of deformation related to magmatic processes detected by the cGPS network prior to, during, or after the 2011 eruption; (3) a relatively steady and high rate of low-frequency (LF: <5 Hz) seismicity during restless periods, transitioning to a sudden drop-off in LF seismicity and a gradually decreasing rate of high-frequency (HF: >5 Hz) seismicity during the months leading up to the eruption; and (4) a possible, though poorly characterized, decrease in both degassing and temperature prior to eruption. These observations suggest that processes other than magma injection triggered the 2011 eruption, and Geirsson et al. (2014) propose that sealing of the hydrothermal system caused a shallow increase in pressure that drove the 2011 explosive activity. Based on the background occurrence of LF seismicity which diminishes or disappears prior to explosions, Geirsson et al. (2014) proposed that sealing of the hydrothermal system caused a shallow increase in pressure that drove the 2011 explosive activity, with individual explosions resulting from catastrophic failure of the seal. Rodgers et al. (2015) noted that the gradual decline in HF seismicity over the 6 months preceding 2011 eruption and the low explosion energy and lack of deformation in 2011 appear to be inconsistent with a strongly sealed system. They suggested that the pressurizing source was shallow and/or embedded in weak or poorly consolidated material. Further, Roman et al. (2016) showed that the duration of precursory seismic quiescence correlates with the energy of the ensuing explosion—consistent with the sealing-pressurizing-failure hypothesis. However, gravity (Locke et al., 2003) and petrographic (Witter et al., 2016) observations from earlier periods suggest that Telica receives periodic new inputs of magma from the midcrust, implying that the 2011 eruption was not entirely representative of Telica's full spectrum of subsurface and eruptive processes.

Here we present multidisciplinary observations of Telica's 2015 eruptive episode, which was significantly more energetic than the 2011 and 1999 episodes. The 2015 eruptive episode included three phases, in April–May, September, and November, each comprising multiple explosions. The May and November explosions launched meter-sized ballistic blocks as far as 1 km away from the vent, endangering local residents, damaging property, killing livestock, and depositing ash on the crater rim and ~40 km downwind toward the west-southwest. We document changes in the volcano's seismic activity leading up to the eruption and present evidence for syneruptive deformation of the edifice, which had not been previously observed at Telica. We suggest that the 2015 eruptive episode was ultimately driven by upward migration of new or previously stagnant magma into the shallow plumbing system. Starting in December 2015, immediately following the most energetic explosion (22 Novembe) in the 2015 sequence, seismicity at Telica was composed of a high but steady rate of LF events, suggesting that the system had returned to a stable (though still restless) state.
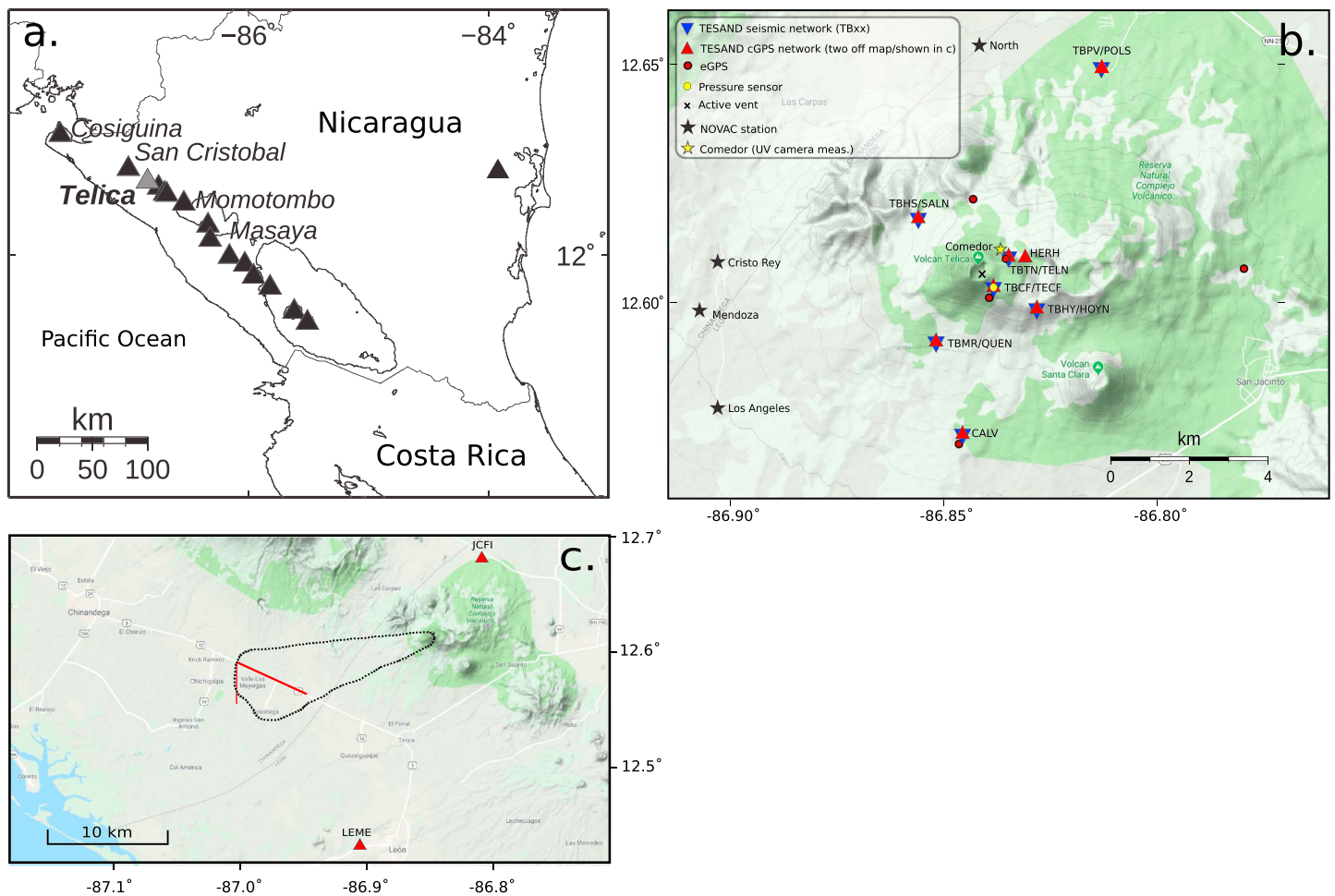
Figure 1. Location of Telica Volcano, instrumentation, and ashfall area in 2015. (a) Holocene volcanoes in Nicaragua (black triangles). Telica Volcano is indicated by a gray triangle. (b) Topographic map of the Telica volcanic complex showing the TESAND network and other instrumentation in place during the 2015 eruption. Seismic and GPS station names are indicated. The active vent is marked with an X. (c) Map of ashfall from the 22 November eruption and locations of local villages/cities. Red lines show approximate routes of differential optical absorption spectroscopy traverses. cGPS stations LEME and JCFI are shown as red triangles. TESAND = Telica Seismic and Deformation; cGPS = Continuous Global Positioning System; NOVAC = Network for Observation of Volcanic and Atmospheric Change.

2. Background

2.1. Telica Volcano

The Telica volcanic complex, located in the Maribios Range of the Central American volcanic arc in western Nicaragua, is an east-west amalgamation of volcanic edifices and nested craters, with the active crater located at the western end of the system (Figure 1). The oldest dated volcanic products associated with Telica are ~330 ka old, and the total volume of eruptive products has been estimated at ~28 km^3, yielding an average extrusion rate of ~10^5 m^3/year (Carr et al., 2007). The oldest historically documented eruption was in 1527 CE (VEI 3), and the only historically documented lava flow is from the 1529 CE eruption (VEI 4). Telica is currently characterized by low explosivity (VEI 1–2) dominantly phreatic explosions every 2–3 years. On decadal time scales, more explosive (VEI 2–4) eruptive episodes occur. During the 1981–1982 eruption, meter-sized blocks were erupted, column heights reached ~4-km altitude, and ash was observed at least 45 km from the volcano, prompting evacuations of the local population (Global Volcanism Program, 1982). In 1994 a series of explosions occurred, with the tallest ash columns reaching ~1.5 km above the crater rim. Major episodes of explosive activity (VEI 2) occurred from May 1999 to February 2000 (Rodgers et al., 2013), in May 2011 (Geirsson et al., 2014), and in 2015 (this study). Between 2000 and 2008 numerous small explosions (VEI 1) were reported. The 2011 eruption of Telica ended on 14 June, and no explosions were

observed at Telica for the remainder of 2011 or in 2012 (Geirsson et al., 2014). Small explosions were reported in January and on 25 September 2013, and no activity was reported in 2014. Incandescence has been observed occasionally in the active vent between 1999 and the present.

Observations of persistent incandescence and long-lived high-temperature fumaroles ($\geq$300 °C) in the active crater indicate the presence of a shallow degassing magma body. Previous workers have found evidence for both deep and shallow magma storage beneath Telica Volcano. LaFemina (1997) investigated changes in soil degassing and temperature related to low-temperature (<100 °C) fumaroles, measuring increases in soil gas Rn and CO_2 and in temperature following phreatic activity in 1994. Locke et al. (2003) collected microgravity data between 1994 and 2000 and found microgravity variations of up to 100 μGal suggestive of a small mass increase at depths of a few hundred meters. Analyses of H_2O and CO_2 in melt inclusions (Sadofsky et al., 2008, T. Plank, pers. comm.) suggest entrapment depths from 2- to 7-km BSL and magma storage at ~7-km BSL. Most recently, based on petrological observations and modeling, Robidoux et al. (2017) proposed that Telica is underlain by two reservoirs at different depths, with the deeper reservoir located more than 5-km BSL. Geodetic studies from 2009 to the 2011 explosive activity did not observe ground deformation associated with episodes of phreatic explosions (Geirsson et al., 2014), and Interferometric Synthetic Aperture Radar (InSAR) deformation surveys of the Central American volcanic arc did not detect deformation at Telica volcano for the period 2007–2017 (Ebmeier et al., 2013; Reath et al., 2019).

2.2. Chronology of the 2015 Eruption

The 2015 eruption of Telica consisted of three main phases, in April–June 2015, September 2015, and November 2015. We describe the main events of each phase below, based on a compilation of direct observations by the authors, newspaper reports, notices of volcanic activity posted by the Washington Volcano Ash Advisory Center, images from a webcam at TELN (Figure 1b), and monthly and weekly reports from the Instituto Nicaragüense de Estudios Territoriales (INETER) published on their website and in the Smithsonian Institution's Global Volcanism Program database.

Phase 1 of the eruption lasted from April 2015 to June 2015. No immediate precursors were recognized in real time. On 8 May 2015, INETER reported that activity at Telica had been increasing, with seven small-intensity explosions detected during an unspecified period. A detailed retrospective analysis of seismic data (see section 3.2) suggests that explosive activity began on 23 April. Large explosions occurred on 8 and 9 May, and an explosion on 10 May appears to have been the first to throw incandescent material out of the vent. INETER staff visited the rim of Telica on 8 May and noted that the 7 May explosions had opened a new vent against the southern crater wall (Figure 2a). An explosion during the night of 11 May ejected several meter-sized bombs a few hundred meters from the vent. Another explosion occurred during the day of 11 May, while a group of tourists were visiting the rim of the volcano (http://www.nbcnews.com/watch/nbc-news/nicaragua-volcano-eruption-caught-on-camera-444623939925). Numerous small and moderate explosions occurred from 11 to 17 May, ejecting hot rock fragments from the crater and generating ash plumes. A lull in explosive activity from 18 to 19 May was followed by a major explosion on 20 May, which deposited ash up to 30 km from the vent and ejected several large incandescent blocks about 400 m from the vent (Figure 2b). At 21:40 local time on 23 May, an explosion ejected 0.5- to 1.0-m diameter blocks as far as 900 m from the vent (A. Longley, personal communication, June 2015). A second large and seismically energetic explosion occurred on 26 May at 11:30 local time, resulting in an ash plume with an altitude of ~4 km (according to the Washington Volcano Ash Advisory Center). During the 26 May explosion, a new ~10-m-wide crater was formed in the northern part of the crater floor (Figure 2c). The new northern crater was later buried by products of the November 2015 explosion. Following the 26 May explosion, numerous small explosions occurred through 6 June, and explosive activity ceased by 8 June. Phase 2 of the 2015–2016 eruption began on 23 September 2015, with a strong explosion that produced a ~4-km-high ash column. Smaller explosions occurred on 24 September. A second strong explosion occurred on 26 September resulting in an ash plume to ~3.6 km and expulsion of rocks of different sizes to as far as 500 m from the crater. During 28–29 September INETER noted that voluminous gas plumes rose from two vents on the crater floor.

Phase 3 of the eruption began on 22 November 2015 at ~09:00 local time, with the most violent explosion in the 2015 sequence. On 21 November, incandescence was observed on the crater floor (Figure 2d). The explosion generated ash plumes that rose ~8 km and ejected large blocks at least 1 km away (Figures 2e and 2f). Blocks ejected during this explosion killed livestock (cows and horses) grazing on the slopes of the volcano
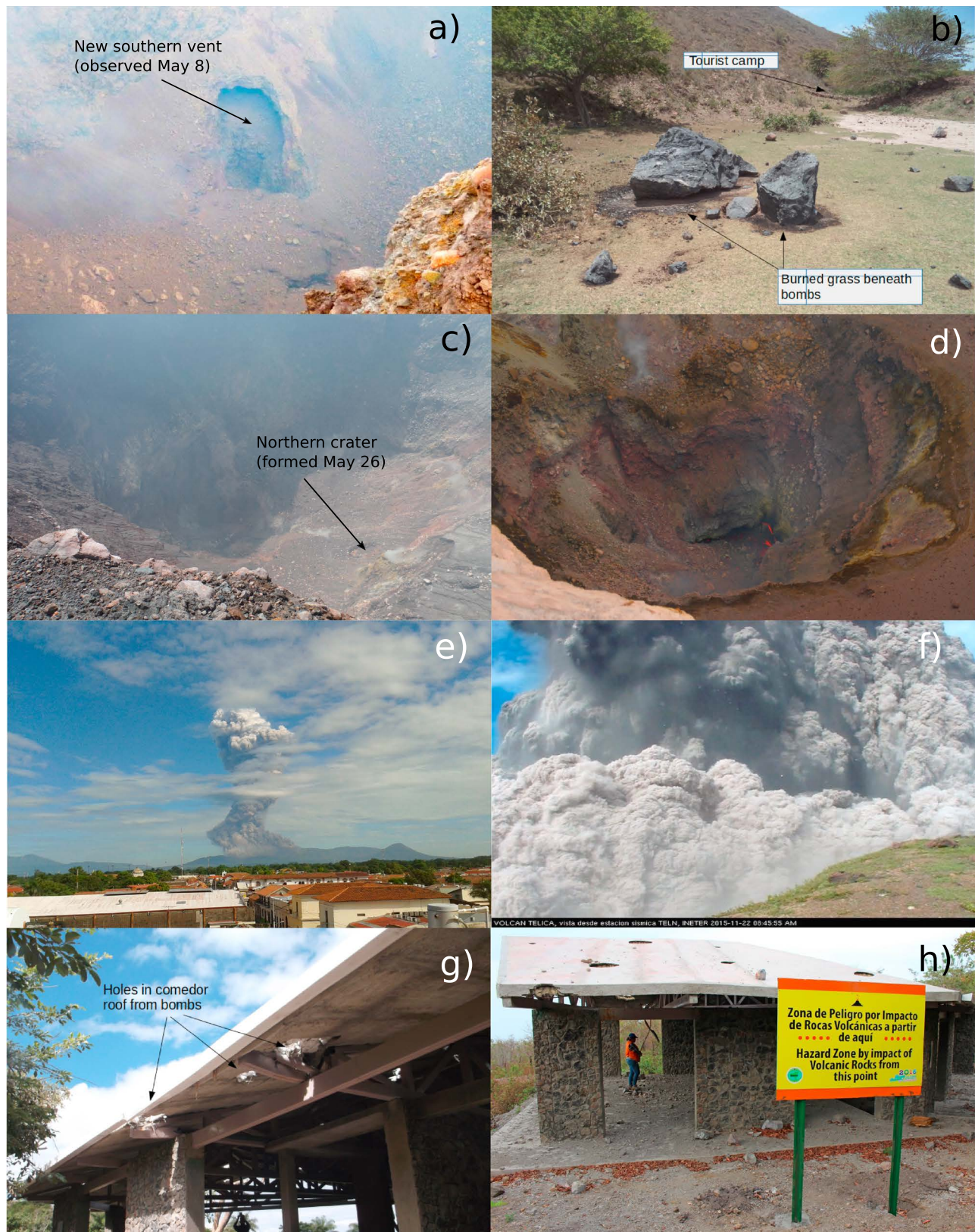
Figure 2. Photos of the 2015 eruption and its effects. (a) New (southern) vent formed by the 7 May explosion. (b) Incandescent blocks ejected during the 20 May 2015 explosions. (c) New (northern) crater formed by the 26 May explosion. (d) Photo of crater on 21 November showing incandescence. (e) The 22 November explosion as seen from Leon. (f) The 22 November as seen from TELN. (g, h) Damage to Comedor (Figure 1) caused by 22 November explosion.
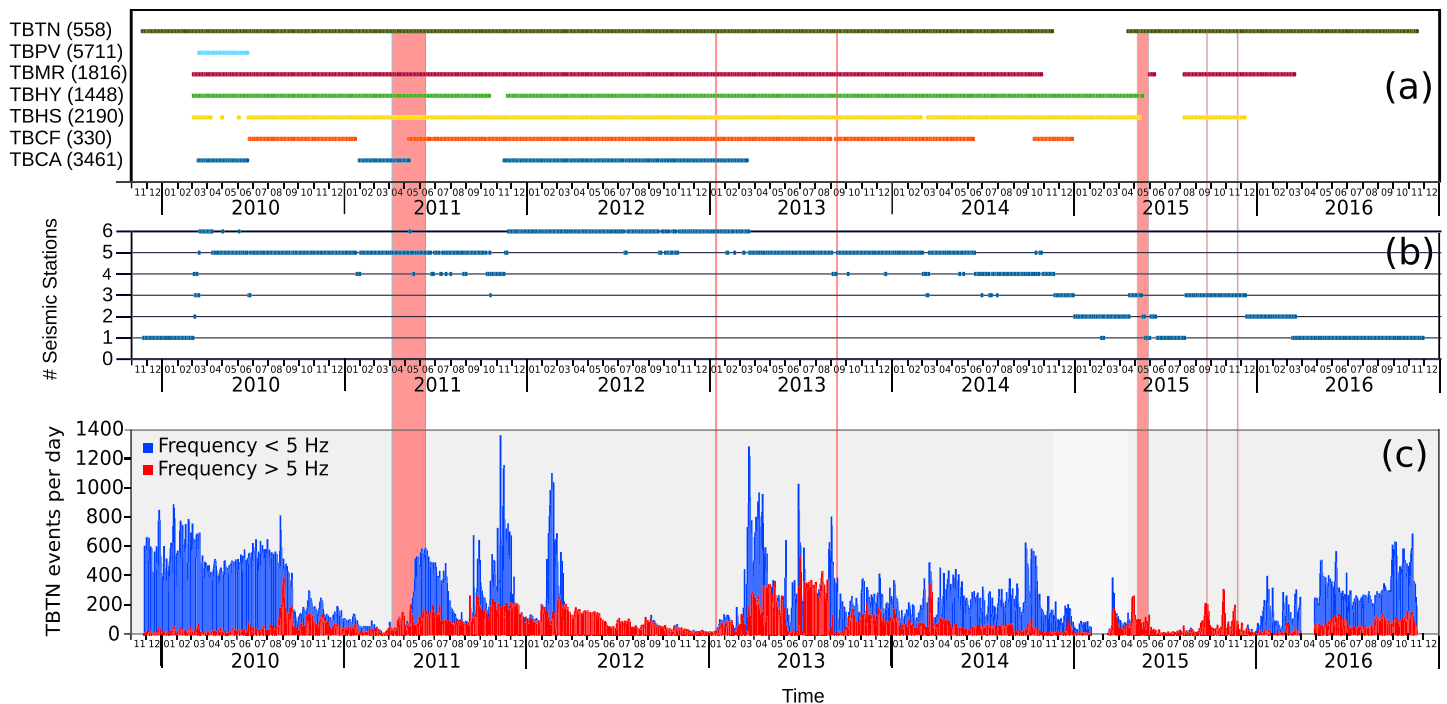
Figure 3. Overview of 2009–2016 TESAND network and seismicity rates. Red vertical bands correspond to periods of eruptive activity. (a) Operation history of each TESAND seismic station (number in parentheses is distance in meters from crater). (b) Number of operating seismic stations over time. Note that only 1–3 stations were in operation in 2015–2016. (c) Number of detected events/day—both high frequency and low frequency. White band shows period when TBTN was out of operation—event counts for this period are from colocated INETER station TELN.

and caused significant damage to an underconstruction concrete building ("Comedor") located on the road up to the volcano (Figures 2g and 2h). Several people living within a 900-m radius evacuated due to the damage to livestock and property. Ash fell in at least 70 communities in the municipalities of Quezalguaque (13 km SW), Posoltega (16 km WSW), Chichigalpa (20 km WSW), and Chinandega (30 km W; Figure 1c). The day before this eruption occurred, there were more than 20 people around the crater rim. Smaller explosions occurred on 25 to 29 November, ending this phase of the eruption.

Residual explosive activity and high-temperature fumaroles were reported by INETER during February–March 2016 and May 2016. On 13 February, an explosion generated a gas plume, possibly containing ash, which rose to an altitude of 1.8 km, and minor explosions were reported on 16 and 17 February. Five gas-and-ash explosions were recorded during 29 February to 1 March, generating plumes that rose 300 m above the crater. Between 7 and 8 May 2016, INETER reported 30 small explosions that generated plumes reaching 600 m above the crater. Later minor explosive activity (VEI 1) was reported by INETER on 10 September 2017 and 21 June to 15 August 2018 (Global Volcanism Program, 2018).

3. Multidisciplinary Observations of the 2015 Eruption

3.1. Seismic Observations

3.1.1. Seismic Network

The seismic component of the TESAND network consisted of one to six broadband seismometers (Guralp 6TD and 6T sensor-digitizer pairs) in operation for approximately 7 years between November 2009 and November 2016 (Figures 1b and 1c and 3a and 3b). Many of these stations were colocated with permanent, short-period sensors operated by INETER. The first station, TBTN, was installed approximately 500 m from the active vent in November 2009. Additional stations were installed between 1.4 and 5.7 km of the vent in March 2010. In June 2010, the farthest station (TBPV) was abandoned and its instrument (a Guralp 6T + DM24 six-channel digitizer) was relocated to a newly constructed site 300 m from the vent (TBCF). TBCF was also equipped with a Chaparral 25V infrasound sensor. Data were recorded on the instruments at 50
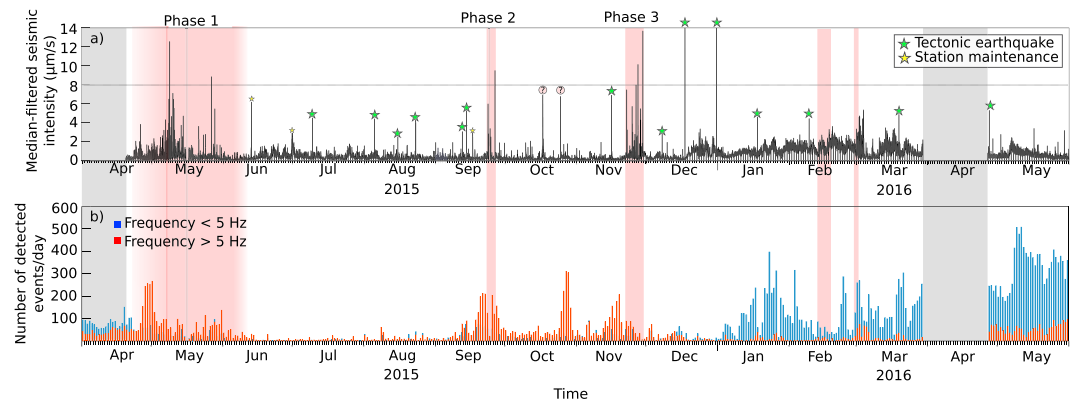
Figure 4. The 2015–2016 seismic intensity and seismic event rates. Red vertical bands are periods of eruptive activity. (a) Median-filtered seismic intensity from April 2015 to May 2016 (see text for details of calculation). Green stars indicate large spikes in seismic intensity due to tectonic earthquakes. Yellow stars indicate large spikes in seismic intensity due to station noise or periods of station maintenance. Two spikes in October 2015 that do not correspond to either tectonic activity or reported eruptive activity are noted with question marks. (b) Number of detected events/day from April 2015 to May 2016—high frequency (red) and low frequency (blue). Gray vertical bands show period when TBTN was out of operation—event counts for this period are from colocated INETER station TELN.

Hz (all 6TD instruments) or 100 Hz (TBCF) and downloaded during periodic maintenance and observation visits. The network began to degrade in mid-2014, and by November 2014, only one to three of the instruments were still in operation, precluding us from locating any seismic events during the 2015–2016 eruption. In December 2015 to March 2016, two of the remaining instruments were permanently relocated to nearby Momotombo Volcano to record activity related to its eruption, leaving TBTN as the only operating broadband seismic station on Telica. Here we only analyze and present data from station TBTN as it was the longest and most continuously running station in the TESAND network. Station TBTN was out of operation from 18 November 2014 to 18 April 2015. For this period, we present limited analyses (event counts) of continuous waveform data from colocated INETER seismic station TELN, which is equipped with a Sara GS11D-3D sensor (4.5 Hz) sampled at 100 Hz. Station TELN was out of operation from 5 February to 10 March 2015; thus we have no seismic data for this period.

3.1.2. Daily Earthquake Rates 2009–2016

We extend the single-station daily event rate counts presented in Rodgers et al. (2015); their Figure 4) through November 2016. The vertical component of the continuous seismic data from TBTN (or TELN) was first high-pass filtered at 0.5 Hz to remove microseismic noise, and an STA/LTA event detection algorithm (AECAP, Powell, 2004) was used to detect events (detection parameters are listed in Table 1 of Rodgers et al., 2015). For each detected event, AECAP reports the peak frequency of the event waveform, which is then used to classify events as HF (peak frequency above 5 Hz) or LF (peak frequency below 5 Hz).

We report the daily number of HF and LF events recorded during the TESAND deployment in Figure 3c. Following the 2011 eruption, the rate of HF events was relatively high and strong swarms of LF events occurred periodically with no corresponding surface activity. A decline in overall seismic event rate began in March 2012, culminating in a minor explosion in January 2013. Both HF and LF events then increased until a second minor explosion in September 2013. Following the September explosion, the rate of both LF and HF events was elevated and steady through

Table 1
Table of Maximum Crater Floor Temperature Measurements at Telica Between 2013 and 2016

Date	Maximum temperature
01/01/13	352
02/01/13	373
03/01/13	455
04/01/13	388
05/01/13	498
06/01/13	479
07/01/13	493
08/01/13	315
09/01/13	456
10/01/13	392
11/01/13	373
12/01/13	355
01/01/14	379
02/01/14	417
03/01/14	438
04/01/14	448
05/01/14	417
06/01/14	372
07/01/14	350
02/01/15	123
04/01/15	412
05/01/15	150
07/01/15	298
08/01/15	50–160
11/01/15	400
03/01/16	485

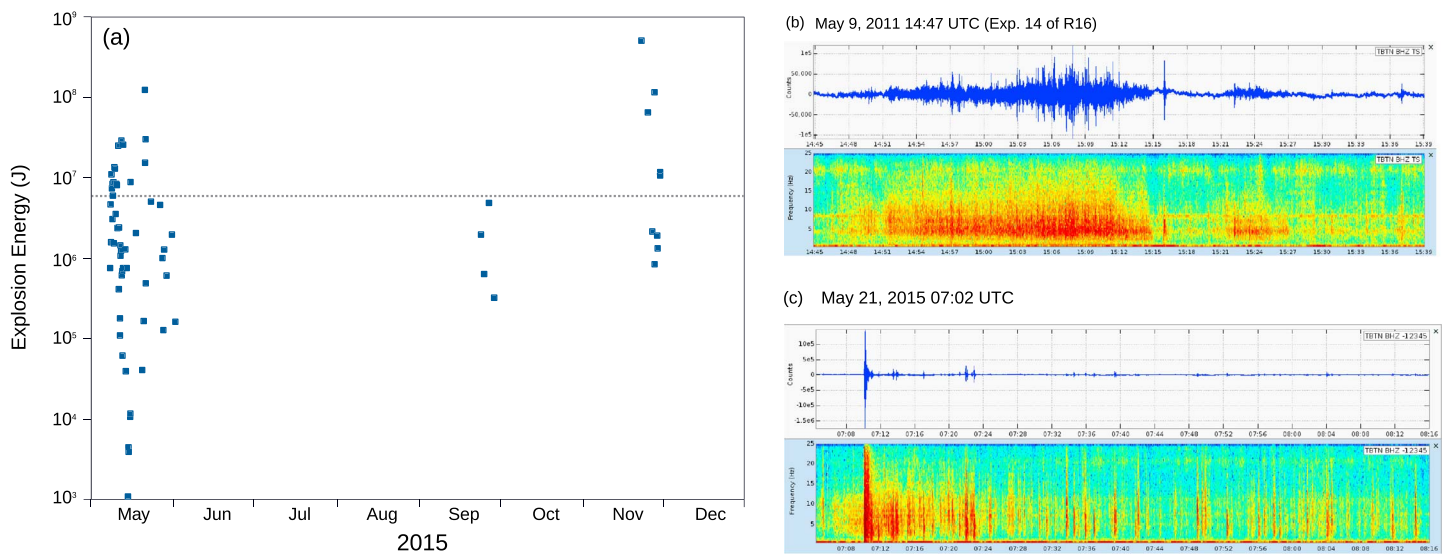*Note.* Dates are formatted as MM/DD/YYYY.

Figure 5. Comparison of 2011 and 2015 explosion energy and explosion waveforms. (a) Plot of explosion energy versus date for 68 explosions in 2015 (note that *y* axis is logarithmic). Horizontal dashed line show maximum explosion energy in 2011. (b) Waveform of an explosion on 9 May 2011. (c) Waveform of an explosion on 21 May 2015.

November 2014 (when TBTN failed), and seismicity was dominated by LF events. From November 2014 to February 2015, HF rates were low and LF rates were declining. After TELN was restored in March 2015, a brief swarm of both HF and LF events occurred. Shortly after TBTN was restored in April 2015, a small swarm of HF events began immediately prior to the onset of the 2015–2016 eruption, from 28 April to 3 May, then continued at a decreased (but still elevated) rate until 14 June 2015. Additional HF swarms were detected in September 2015, immediately prior to Phase 2 of the eruption, in October 2015 (not associated with explosive activity; see below), and in late November immediately prior to the onset of Phase 3 of the eruption. The rate of LF events remained extremely low from April through the end of 2015. LF activity increased suddenly in January 2016 (not directly correlated with explosive activity) and remained at an elevated but steady rate through the remainder of the study period, accompanied by moderate rates of HF events.

3.1.3. Earthquake Rates and Seismic Intensity: April 2015 to May 2016

As an additional first-order assessment of seismic and volcanic activity during the 2015–2016 eruption, we calculate and assess a continuous median-filtered seismic intensity time series (Figure 5), which is a measure of the total seismic energy release from all sources, including volcanic earthquakes, volcanic explosions, tectonic earthquakes, and noise sources (i.e., analogous to RSAM). Raw seismic records from the vertical component (BHZ) of TBTN were band-pass filtered from 0.5 to 20 Hz and converted to velocity seismograms (following Haney et al., 2012). Following Taisne et al. (2011), the envelope of each seismogram was calculated by taking the absolute value of the Hilbert transform of the seismogram and then smoothing it using a 15,000-point (5 min) median filter (Figure 5a). Some of the spikes in seismic intensity correspond to moderate- or large-magnitude tectonic earthquakes—these are noted in Figure 5a.

Calculated seismic intensity largely mirrors earthquake rates (Figure 5b) over time. In 2015, the seismic intensity curve shows a very low background level, corresponding to a low rate of seismic events (Figure 5b), particularly between Phases 1 and 2. Starting in mid-December 2015, the background level increases, corresponding to an increase in the rate of LF seismic events. Seismic intensity is strongest during the three main eruption phases, with sharp peaks in the seismic intensity time series correlated with major explosive events described in section 2.2. The largest explosions in terms of peak seismic intensity occurred on 8 May 2015 and 29 November 2015. These and three other explosions, on 26 May, 26 September, and 26 November 2015, each produced more seismic energy than the largest explosion in the 2011 sequence as measured by Roman et al. (2016), the peak energy of which is indicated by the horizontal dashed line in Figure 5a. Interestingly, two moderately strong spikes occurring in October 2015 (the second
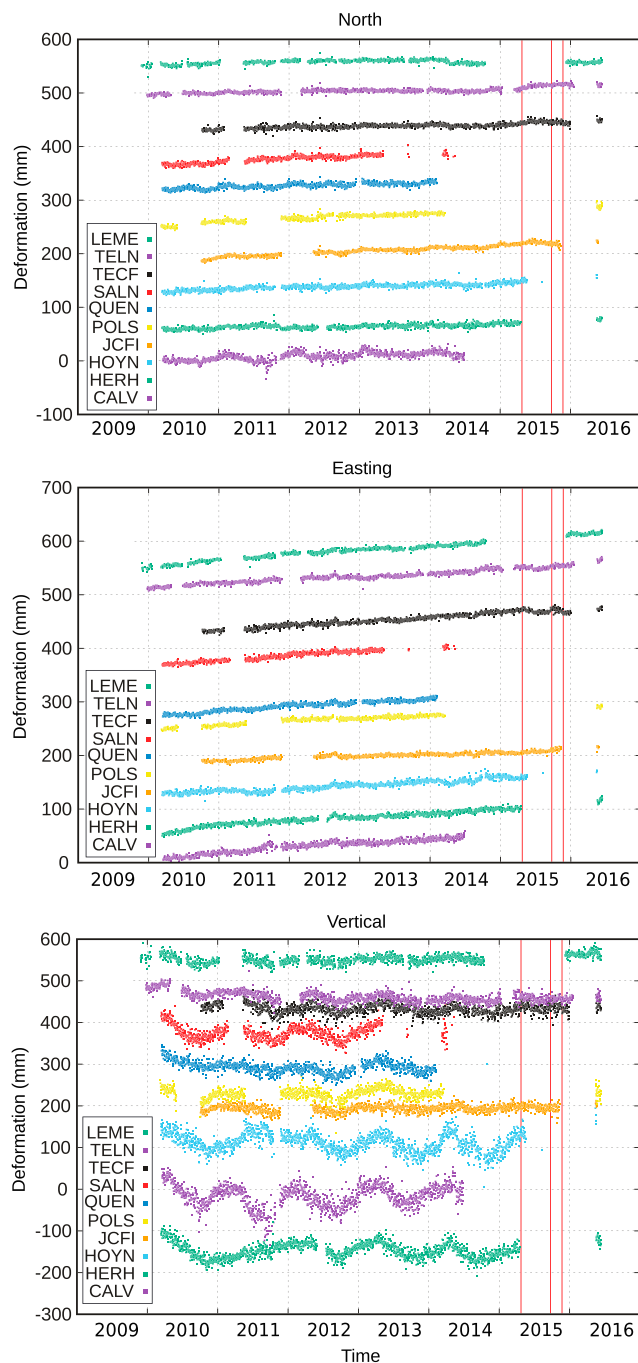
Figure 6. TESAND continuous Global Positioning System time series in the ITRF2008 reference frame from ~2009/2010 to 2016.5. Note that most of the network was running up to 2014. The long-term, horizontal motion of the TESAND network is caused by northwest directed forearc motion. Note that stations TECF, TELN, and JCFI (Figure 1) were the only sites running during the eruptive episode.

corresponding to the beginning of an HF swarm) do not correspond either to tectonic earthquakes or reported explosions at Telica. The seismic signal underlying these spikes is tremor like and similar to signals during confirmed explosions in this sequence. Thus, these two spikes may represent additional unreported explosions or perhaps shallow unrest with no surface expression.

3.1.4. Explosion Energy

The observation that several 2015 explosions exceeded peak seismic intensity of the largest 2011 explosion prompts a more detail comparison of the two eruptions. Roman et al. (2016) calculated explosion energy for 50 explosions comprising the 2011 eruption following the method of Johnson and Aster (2005) and found that integrated energy released in individual explosions ranges from 1×10^5 to 6.07×10^6 J, with an average of 1.8×10^6 J. Using the same approach, we calculate explosion energy for 68 confirmed explosions during Phases 1–3 of the 2015 sequence and find that integrated energy ranges from 1×10^3 to 5×10^8 J, with an average of 1.7×10^7 J, an order of magnitude higher than the average energy release during the 2011 eruption (Figure 6a). Furthermore, we note a marked difference in the overall shape of the explosion waveforms between 2011 and 2015. To illustrate this difference, we show explosion seismic waveforms in the time and frequency domains for a representative 2011 explosion (9 May 2011—explosion 14 of Roman et al., 2016; Figure 6b) and a representative 2015 explosion (21 May 2015; Figure 6c). The waveforms of the 2015 explosions begin with a strong, impulsive broadband pulse and decays fairly quickly (within 1–2 min). In contrast, the 2011 explosion waveforms are generally emergent and sustained, suggesting different explosion mechanisms for the two eruptions.

3.2. Geodetic Observations
3.2.1. CGPS Observations

GPS observations of Telica volcano began in August 1999 following explosive activity, with the installation of a three-site episodic GPS network. The continuous GPS component of the TESAND network consisted of 10 stations. Station TELN was installed in 2009 at INETER TELN seismic hut (i.e., location of TBTN broadband seismic sensor) and approximately 2 m from episodic GPS station TELI installed in 1999. The 10-station network (Figures 1b and 1c) was completed in 2010 and ran fairly continuously through 2014, with several stations running through 2018 (Figure 4; supporting information Figures S1 and S2). Each station consisted of either a Trimble NetRS or NetR9 receiver, and a Trimble Zephyr Geodetic II antenna mounted on a 0.5-m stainless steel rod bolted, epoxied, and cemented into the roof of the concrete seismic huts. Data were transmitted from most stations to the INETER seismic network station at Telica north (TELN) via wifi or radio telemetry and then on to INETER offices in Managua for upload to UNAVCO. During the 2015–2016 eruptive phase, three stations were running, TELN, TECF, and JCFI, located ~500 m, ~200 m, and ~8.5 km, respectively, from the active vent.

We produced daily position estimates for each GPS station using GISPY OASIS II software version 6.3 and precise clock and orbit products provided by the Jet Propulsion Laboratory (Zumberge et al., 1997). We use final orbit and clock products from the Jet Propulsion Laboratory and obtain daily positions in the International Terrestrial Reference Frame 2008 (Altamimi et al., 2011). Position time series and baselines between network sites are then estimated to investigate tectonic and magmatic deformation signals. The long-term horizontal components of the
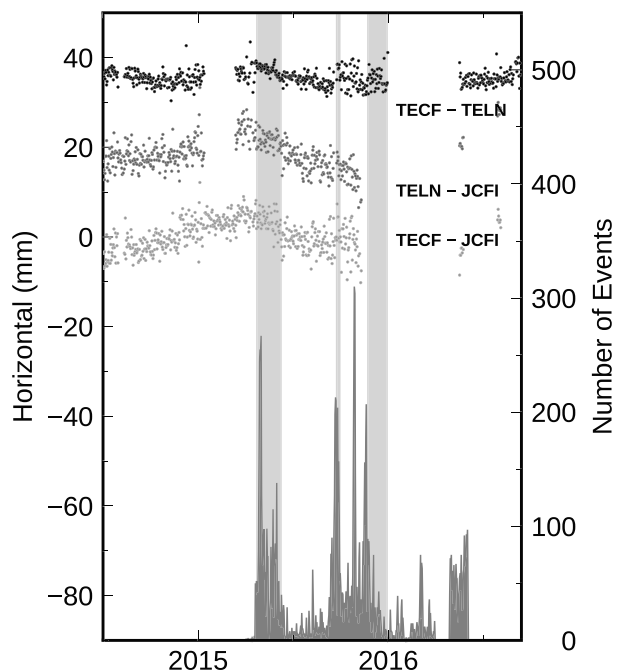
Figure 7. Continuous Global Positioning System station baselines for the three stations operating during the 2015–2016 eruptive episode. The first station is plotted relative to the second station. The gray bars are the three eruptive phases as discussed in the text. See text for discussion of the time series. Vertical gray bars show total number of seismic events per day during this period.

daily time series are dominated by translation of the Nicaraguan forearc toward the northwest, and the horizontal and vertical components are affected by annual and semiannual signals (Figures 4 and S1).

To investigate potential deformation of Telica volcano correlated with 2015–2016 explosive activity, as well as the other observations presented here, we interrogated changes in baseline length between TECF and TELN (~520-m baseline). Additionally, we estimated baselines between JCFI and TECF (8.6 km) and TELN (8.2 km) for the first two phases of explosive activity (Figure 7; station JCFI ceased operation just before the third phase of explosive activity). The baselines and long-term time series indicate steady motion leading up to the eruptive episode. However, with the onset of Phase 1, the TECF-TELN baseline appears to coeruptively extend and then contract, continuing to do so until the onset of Phase 2 in September. With the initiation of Phase 2, the TECF-TELN baseline instantaneously extends again and then contracts until Phase 3. In fact, all three baselines show potential coeruptive deformation (baseline extension) associated with Phase 2 of the eruptive episode, followed by contraction. The TECF-TELN and TECF-JCFI baseline time series become noisier after Phase 2 explosive activity, and the JCFI baselines end in October, making it difficult to correlate the October 2015 HF seismic swarm with deformation of the edifice. In total, the TECF-TELN baseline shortens by <1.0 cm, and the TECF-JCFI and TELN-JCFI baselines shorten by <1.5 cm during the 2015 eruptive episode. On 22 November 2015 meter size volcanic bombs impacted the ground around the hut. Nevertheless, the antenna continued to function.

3.2.2. InSAR Observations

To investigate whether there was a broader distribution of deformation at Telica, we processed InSAR ground deformation maps (or differential interferograms (e.g., Hanssen, 2001; Massonnet & Feigl, 1995; Simons & Rosen, 2015)) around the 2015 eruptive phase. All interferograms were processed using the GAMMA software (Werner et al., 2000), with topographic phase contributions removed using a 12-m TanDEM-X DEM (Rizzoli et al., 2017; Wessel et al., 2018).

InSAR images from Sentinel-1 spanning the eruptive period confirm the GPS deformation signals (Figure 8). Sentinel-1 is a C-band (wavelength ~6 cm) satellite with ~15-m spatial resolution. A descending pair of images covering December 2014 to early May 2015 (Figure 8a) shows motion toward the satellite of less than ~1.5 cm, consistent with coeruptive baseline extension for Phase 1 of the eruptive episode (Figure 7). A descending pair of images spanning May–November 2015 (Figure 8b) shows motion away from the satellite of ~1.5 cm, consistent with baseline contraction following initiation of 2015 eruptive activity in April 2015 (Figure 7).

For a more detailed view of deformation at Telica during the 2015–2016 eruption sequence, we analyzed data from COSMO-SkyMED (CSK), a constellation of four X-band (3.1 cm) satellites with a ~1-m spatial resolution and a higher temporal resolution than Sentinel-1. We analyze a data set of 50 CSK descending SAR images and construct time series of deformation patterns at Telica during 2015. Wrapped and unwrapped interferograms were created for 199 pairs corresponding to small perpendicular and temporal baseline interferograms and then inverted to find the least squares solution for the line-of-sight displacement for each time period between consecutive CSK images at each pixel following the Small Baseline Subset approach (Berardino et al., 2002; Lundgren et al., 2001). Pixels with a coherence of less than 0.5 were discarded from the analysis. The resulting InSAR time series at the location of cGPS station TECF (Figure 9) closely matches the line-of-sight projection of the East, North, Up components of the GPS station. The comparison validates the InSAR and GPS measurements; however, it clearly shows the annual and semiannual signals in both time series that make it difficult to study the low-magnitude deformation at Telica Volcano (Figure 9).

S1_141220_150501
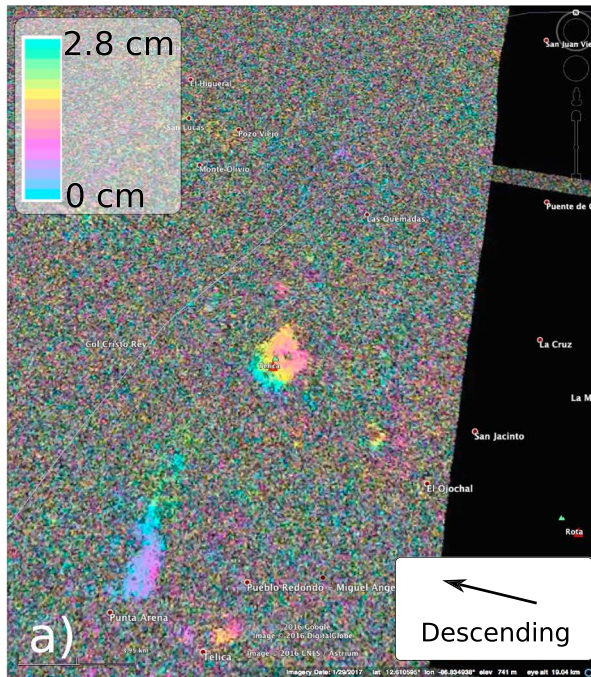
S1_150426_151104
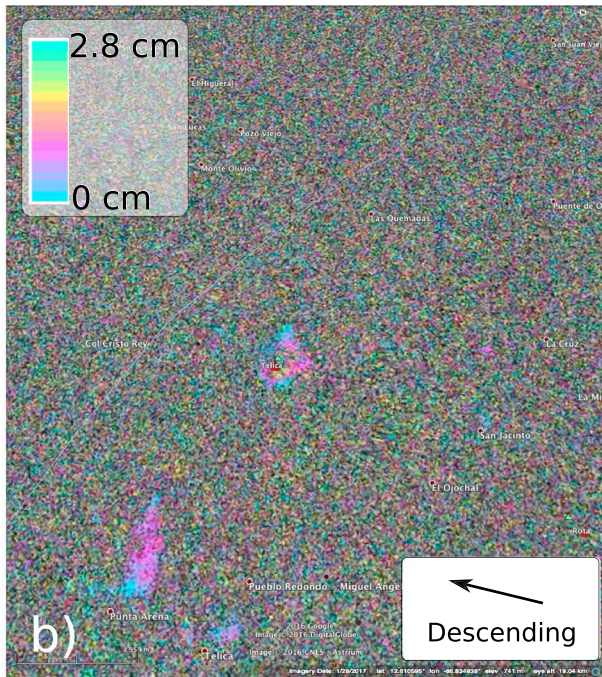
S1_150426_151104
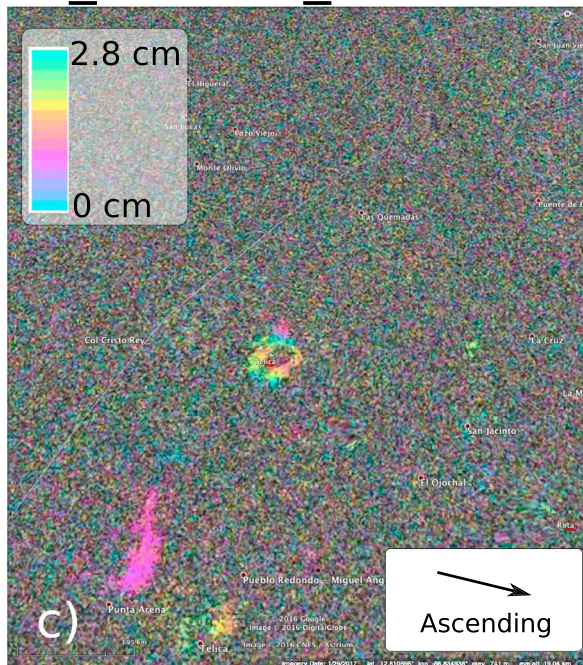
Figure 8. Sentinel-1 interferograms spanning the 2015 unrest. (a) Descending pair from 20 December 2014 to 1 May 2015 showing less than ~1.5 cm (half a fringe) of line-of-sight (LOS) uplift, consistent with GPS NE motion (Figure 7). (b) Descending pair from 26 April 2015 to 4 November 2015 showing less than ~1.5 cm (half a fringe) of LOS subsidence consistent with Global Positioning System SW motion (Figure 7). (c) Ascending pair from 26 April 2015 to 4 November 2015 ~1.5 cm (half a fringe) of LOS uplift consistent with Global Positioning System SW motion (Figure 7).

Figure 9. Time series of deformation at Telica at the location of the GPS station TECF (Figure 1). Black dots are the Interferometric Synthetic Aperture Radar COSMO-SkyMED descen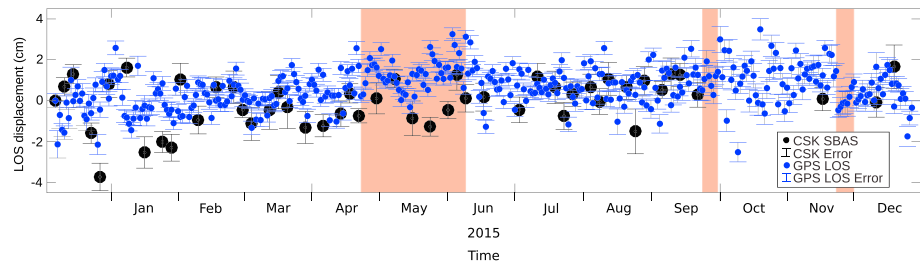ding time series range line-of-sight (LOS) displacements, while the blue dots are the TECF [E,N,U] displacements projected into the COSMO-SkyMED LOS geometry (LOS vector: [0.5238−0.1025 0.8456]). Reference for the Interferometric Synthetic Aperture Radars time series is (12.5737, −86.8610). GPS = Global Positioning System.

3.3. SO₂ Gas Flux

Flux of SO_2 from the summit vent has been measured periodically at Telica volcano by several independent research groups, using a variety of instruments and methodologies. Here we report on previously published and new measurements of SO_2 flux collected from 2010 to 2016, including the first measurements of SO_2 flux immediately before and after a major explosion at Telica (originally reported in de Moor et al., 2017). In summary, the SO_2 flux during pre-2015 background periods was ~13–335 tons/day (t/day). One day before a major explosion (on 21 November 2015), the SO_2 flux was found to be negligible (i.e., below the detection limit of the method, estimated to be ~5 t/day for the conditions under which the measurement was conducted), and immediately following the 22 November explosion, SO_2 flux was relatively high (1,100–1,600 t/day). From December 2015 onward, background SO_2 flux appears to have stabilized around the pre-2015 background level at ~19–454 t/day.

Only a few pre-2010 measurements of SO_2 flux at Telica have been reported in the literature. Andres and Kasgnoc (1998) report a mean flux of 84 t/day for the period 1972–1997. Mobile traverses using portable ultraviolet correlation spectrometers reported 41 t/day in March 1996 (Global Volcanism Program, 1996) and between 50 and 500 t/day during an eruptive period at Telica in November 1999 (Global Volcanism Program, 2000). Mobile differential optical absorption spectroscopy (DOAS) measurements conducted on 30 November 2003 during a noneruptive period gave values of 250 to 1,250 t/day with an average of 530 ± 120 t/day (± corresponding to 1 standard deviation; Mather et al., 2006).
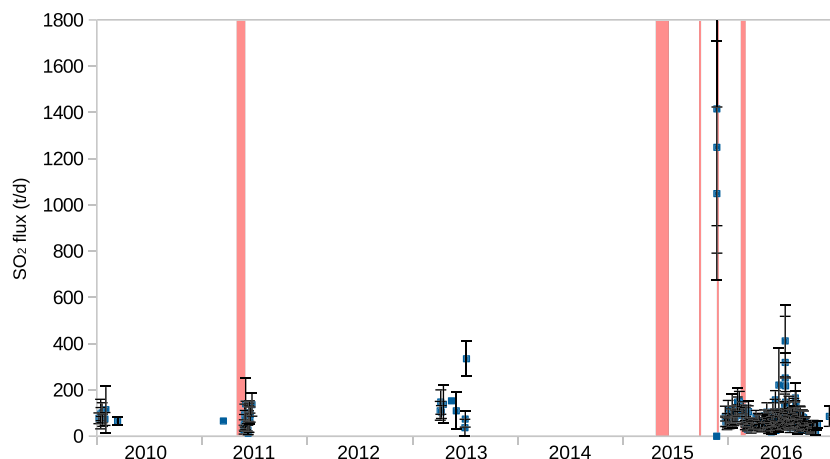

Figure 10. Time plot of published and new gas measurements 2010–2016. Vertical red bands show the timing of the 2011 eruption, Phases 1–3 of the 2015 eruption, and a period of residual activity in 2016. See Table S1 for underlying data and sources. Vertical bars show daily variability in measurements.
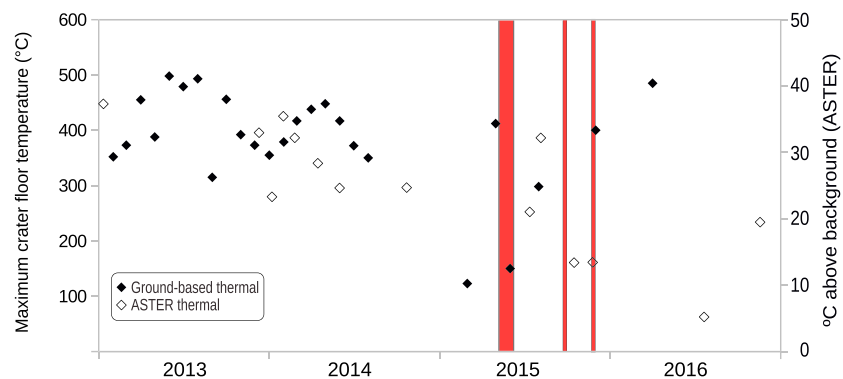
Figure 11. Plot of maximum temperature measurements over time. Vertical red bands are Phases 1–3 of the 2015 eruption. Thermal anomalies estimated from ASTER satellite data in degrees Celsius above background in open diamonds (Reath et al., 2019). Ground-based measurements of maximum crater floor temperature measurements at Telica in Celsius in filled diamonds.

In the 5 years preceding the 2015 eruption (2010–2014), reported SO_2 emissions were relatively low, ranging from 13 to 335 t/day (Table S1 and Figure 10), with an average of 93 t/day. This degassing rate remained steady even during the penultimate eruptive event in May 2011 (Global Volcanism Program, 2011). Conde et al. (2014) describe measurements obtained using a rapid deployment system for volcanic gas monitoring that employs optical scanning DOAS instruments (Conde et al., 2014). They report background levels of 115 ± 100 t/day for a quiescent period from 20 January to 27 March 2010, 140 ± 110 t/day during the 2011 eruption episode, 64±34 t/day in March 2013, and 110 ± 80 t/day from May–June 2013. Geirsson et al. (2014) report a mobile DOAS measurement of 66 t/day on 16 March 2011. Measurements from a daily scanning DOAS located at four sites around Telica (Figure 1b), part of the Network for Observation of Volcanic and Atmospheric Change (Galle et al., 2010), operated by INETER (Saballos et al., n.d.) range from 13 ± 5 to 335 ± 75 t/day (these measurements were calculated using wind data from the ECMWF ERA-interim database, interpolated to the time of measurement and position of the plume). On 9 May 2013, an SO_2 UV camera was deployed on the north flank of Telica (Comedor location in Figure 1b) for approximately 1 hr, and SO_2 flux and plume speed were calculated several times per minute, using an estimated wind speed of 4 m/s. SO_2 flux during the scan ranged from ~50–350 t/day, with an average value of 153 t/day.

No measurements of SO_2 were made between August 2013 and October 2015. On 21 November 2015, less than 24 hr before the largest vulcanian explosion of the 2015 sequence, a group of INETER and OVSICORI-UNA volcanologists working on the crater rim of Telica simultaneously and consistently measured a negligible SO_2 flux of <5 t/day by both mobile DOAS walking traverse (de Moor et al., 2017) and by stationary FLYSPEC V2. Several DOAS traverses were made from a car along a gravel road running N-S between Chichigalpa and Posoltega, about 5 km west of the volcano (Figure 1c) on 22 November 2015 hours after the explosive eruption. During these traverses, the plume was ash free and uncondensed. Overhanging trees along the road affected many spectra, which were filtered out. The SO_2 flux was found to be 1049 ± 375–1,415 ± 505 t/day.

Following the end of the eruption, from 21 December 2015 through the end of 2016, daily scanning DOAS from La Mendoza gave a range of 19–165 t/day, averaging 66 t/day. Driving mobile DOAS measurements in April–July 2016 were made along the main highway between Leon and Chinandega (Figure 1c), allowing rapid transects with little tree interference; the plumes were broad and dilute. During this period, the SO_2 flux ranged from 59 to 412 t/day, with an average of 233 t/day (de Moor et al., 2017).

3.4. Thermal Measurements

INETER periodically monitors the temperature of Telica's inner crater using a Testo 820 infrared pyrometer or a FLIR SC620 thermal camera, recording the hottest point in the crater visible from the crater rim (Table 1). In 2013 and early 2014, thermal measurements were taken almost daily. Beginning in mid-2014, temperature measurements became more sporadic, with only one or two measurements reported per month. We plot reported temperatures in Figure 11. In addition, we plot ASTER thermal anomaly

Table 2
Ash Samples Collected for This Study

	Sample	Sample date	Location	Sampling notes
Leachates/XRD	TEL160511	05/16/11	0.8 km ENE of crater rim	Collected from metal farmhouse roof
Leachates/XRD	TEL180511	05/18/11	50 m from crater rim	Tarpaulin sample, 16–18 May cumulative
Leachates/XRD	TEL210511	05/21/11	0.8 km ENE of crater rim	Sample bucket
Leachates/XRD	TEL210515	05/21/15	2.5 km W of crater rim	Shaken off leaves and plants by roadside
Leachates/XRD	TEL220515a	05/22/15	Crater rim	Ground sample collected at crater rim
Leachates/XRD	TEL220515b	05/22/15	2 km SW of crater rim	Ground sample collected at GPS/Seismic Station QUEN
Modal analysis	Te151121A1	11/21/15	Crater rim	September eruption
Modal analysis	TE151122A1	11/22/15	12.608033, −86.860500	Dry, no fine ash, very big fragments
Modal analysis	TE151122A2	11/22/15	12.608033, −86.860500	Dry, collected over 10 × 10 cm
Modal analysis	TE151122A3	11/22/15	12.608033, −86.860500	Dry
Modal analysis	TE151122A4	11/22/15	12.608033, −86.860500	Dry
Modal analysis	TE151122A5	11/22/15	12.601417, −86.870750	Dry, collected from ground
Modal analysis	TE151122A6	11/22/15	12.601417, −86.870750	Dry collected from plants
Modal analysis	TE151122A7	11/22/15	12.601417, −86.870750	Dry collected from plants
Modal analysis	TE151122A8	11/22/15	12.601850, −86.874867	Dry collected from plants
Modal analysis	TE151122A9	11/22/15	12.600150, −86.884967	Dry collected from plants
Modal analysis	TE151122A10	11/22/15	12.600150, −86.884967	Dry collected from plants and ground
Modal analysis	TE151122A11	11/22/15	12.602600, −86.901533	Dry, collected over 10 × 10 cm
Modal analysis	TE151122A12	11/22/15	12.602600, −86.901533	Dry collected from tomb
Modal analysis	TE151122A13	11/22/15	12.606617, −86.924033	Collected from metal farmhouse roof
Modal analysis	TE151122A14	11/22/15	12.606617, −86.924033	Collected on a pile
Modal analysis	TE151122A15	11/22/15	12.606617, −86.924033	Collected on water dish
Modal analysis	TE151122A16	11/22/15	12.599067, −87.003717	Collected on plastic
Modal analysis	TE151122A17	11/22/15	12.596133, −87.020600	
Modal analysis	TE151122A18	11/22/15	12.596133, −87.020600	Collected on plastic canvas
Modal analysis	TE151122A19	11/22/15	12.602283, −87.017283	Collected from banana leaf
Modal analysis	TE151122A20	11/22/15	12.607100, −87.013800	Collected on plastic canvas
Modal analysis	TE151122A21	11/22/15	12.607100, −87.013800	Collected on plastic canvas
Modal analysis	TE151122A22	11/22/15	12.668417, −87.165867	Collected from papaya leaf
Modal analysis	TE151122A23	11/22/15	12.668417, −87.165867	Collected from vehicle

Note. Dates are formatted as MM/DD/YYYY. XRD = X-ray diffraction.

measurements for 2013–2016 from Reath et al. (2019). Average maximum crater floor temperatures between January 2013 and July 2014 range from ~300 to 500 °C and reflect seasonal variations. Following a period of 7 months during which no thermal observations were made, INETER reported a single-day maximum thermal measurement of 123 °C for 25 February 2015, lower than any single-day measurement reported in 2013 or 2014. A "normal" measurement of 412 °C was reported for April 2015, followed by two more "low" measurements of 149.4 and 150.2 °C on 8 May and a higher measurement of 377 °C on 14 May. Three further measurements during the second half of 2015 and 2016 indicate steadily increasing temperatures from 300 to 500 °C, within the range of the seasonally modulated pre-2015 background range. ASTER measurements suggest that temperatures increased after Phase I and were low between Phases II and III. Although these measurements are from techniques/instruments with different sensitivities and errors, they combine to present a general overview of thermal unrest at Telica over our study period.

3.5. Ash Analysis

We collected and analyzed ash samples from four different eruption dates: (1) Samples of explosions between 16 and 18 May 2011 (previously reported in Geirsson et al., 2014) were collected from 0.8 km ENE of the crater and from a tarpaulin left 50 m from the crater rim over these 3 days; (2) samples of the 20 May 2015 eruption were collected on 21 May from ~2 km west of the crater rim (shaken off of leaves of plants on the side of the road); (3) samples of the September eruption were collected from the crater rim on 21 November 2015; and (4) samples of the 22 November eruption were collected at various distances from the crater on 22 November 2015 (Figure 1c). Ash samples (Table 2) were analyzed for ash leachate compositions, X-ray diffraction (XRD), and to estimate the relative proportions of mineral components in tephra
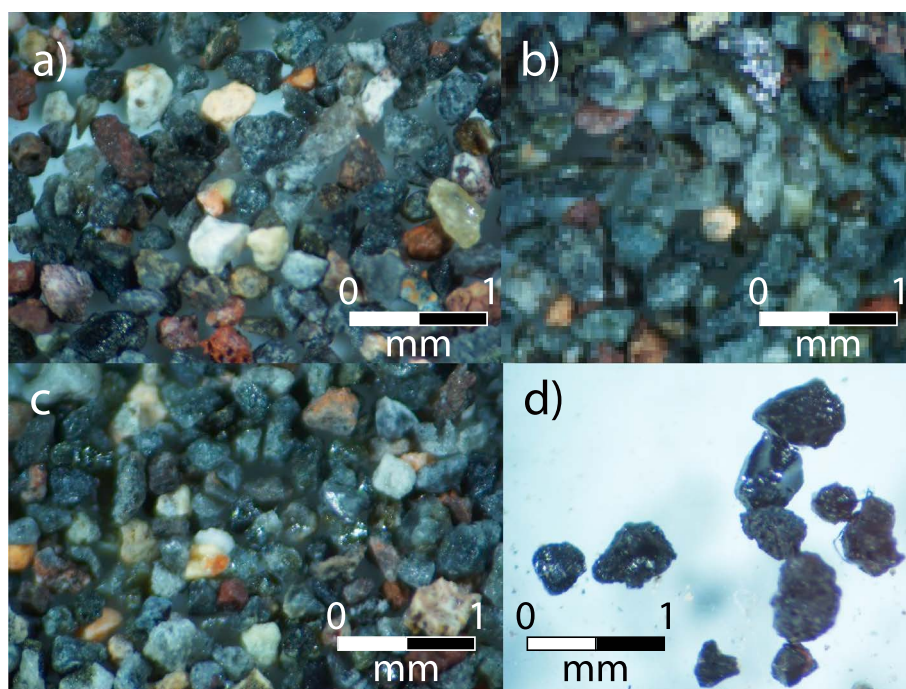
Figure 12. Photos of ash samples used for point counting: (a) Te151121A1, (b) Te151122A5, (c) Te151122A12, and (d) Te151121A1 fresh glass fraction.

clasts (modal analysis). Trace amounts of juvenile glass shards were observed in ashes sampled on 21 and 22 November and associated with Phase 2 (Figure 12 and Table 3) but account for 10% or less of the 250- to 500-μm size fraction. Accretionary lapilli were observed in 2015 ash samples, as was the case for the 2011 eruption. Ash samples were analyzed at The Pennsylvania State University (XRD and ash leachate analysis) and at OVSICORI (mineral modal ash analysis).

3.5.1. Ash Leachate and XRD Analyses

Ash leachate analysis procedures followed the guidelines of Witham et al. (2005). Ash leachate analyses allow for an independent estimate of the concentration of gas species in eruptive plumes, offer insights into the eruptive products (e.g., eruption of hydrothermally altered rocks and/or deposited mineral species; Taylor & Stoiber, 1973), and the potential environmental impacts of trace element metal and halogen deposition. One gram of ash was added to 25 ml of deionized water and agitated for 90 min. The samples were then centrifuged (4,000 g at 20 °C) for 10 min. Solid residue was separated from the leachate using a 0.45-μm nylon filter. Major elements (Na, K, Ca, Mg, Al, Mn, and Fe) were analyzed in the leachates using a

Table 3
Modal Mineral Analyses Following Sieving in 250- to 500-μm (Micrometer) Fraction, Given as Point Counts (Top) and Percentages of Total Counts (Bottom)

	Dates		Scoria/lava			Free crystals			
Name	Sampling	Eruption	Strongly Altered	Partly Altered	Fresh	Olivine	Translucent	Other	Total
Point counts									
Te151121A1	2015/11/21	September	152	728	107	10	9	28	1034
Te151122A5	2015/11/22	2015/11/22	171	788	119	5	4	24	1111
Te151122A12	2015/11/22	2015/11/22	206	749	48	0	4	18	1025
Percentages of total counts									
Te151121A1	2015/11/21	September	14.7	70.4	10.3	1	0.9	2.7	100
Te151122A5	2015/11/22	2015/11/22	15.4	70.9	10.7	0.5	0.4	2.2	100
Te151122A12	2015/11/22	2015/11/22	20.1	73.1	4.7	0	0.4	1.8	100

Note. See text for a definition of the six categories. Dates are formatted as YYYY/MM/DD.

Table 4

Ash Leachate Analyses Reported in Milligrams of Solute per Kilogram Ash and Analyzed at an Ash:Water Ratio of 1:25

Sample	SO_4 mg/kg	Cl mg/kg	F mg/kg	Na mg/kg	K mg/kg	Ca mg/kg	Mg mg/kg	Al mg/kg	Mn mg/kg	Fe mg/kg	Zn mg/kg	Cu mg/kg	As mg/kg	Pb mg/kg	Se mg/kg	Ni mg/kg	Cr mg/kg
TEL160511	32,651	2,076	85.4	1,081	172	15,844	589	264	29.9	40.7	7.16	2.15	0.0933	0.00278	0.153	0.419	0.0196
TEL180511	32,072	1,684	81	1,031	3.35	15,149	872	217	42.8	3.35	1.18	1.49	0.0296	0.00035	0.0951	0.678	0.0043
TEL210511	28,275	1,425	70.7	1,087	162	12,708	756	297	36	75.5	2.25	4.19	0.0695	0.00168	0.0609	0.516	0.0324
TEL210515	17,988	795	186	340	191	6,660	430	48.9	20.6	1.25	0.62	1.66	0.0314	0.00028	0.156	0.039	0.0012
TEL220515a	44,893	4,883	270	649	3.6	14,714	2,787	204	155	5.96	8.5	40.5	0.1439	bdl	0.706	1.22	0.0042
TEL220515b	42,351	771	214	598	55.6	14,194	1,429	138	71.9	10.7	3.7	6.66	0.0513	0.00043	0.308	0.447	0.003

Note. bdl = Below Detection Limit.

Perkin-Elmer Optima 5300DV ICP-AES; trace elements (Zn, Cu, As, Pb, Se, Ni, and Cr) were analyzed using a Thermo X-Series II Quadrupole ICP-MS, and SO_2^{4-}, Cl^-, and F^- ionic abundances were analyzed using a Thermo Dionex ICS 2500 ion chromatography system.

Leachates of ash collected during the May 2015 eruption contained notably less Ca, SO_4, Na, and Cl relative to the 2011 eruption but more F (Table 4). Metal concentrations were generally lower than those in the 2011 leachates (Geirsson et al., 2014). One ash sample collected from near the crater rim during the November 2015 eruption had significantly higher leachate concentrations of Cl, F, Mg, Mn, Cu, As, Se, and Ni. Leachates of an ash sample collected the same day (22 November 2015) from a location on the flank had more moderate concentrations broadly comparable to those of the 2011 samples but with lower Na and Cl. Fluorine in all ash leachates exceeds WHO drinking water guidelines at an ash/water ratio of 1:25, while Cu and Ni in the 22 November crater rim sample approach safe drinking water limits (World Health Organization, 2011). The dominant species in the ash leachates, Ca, SO_4, Na, and Cl, are consistent with precipitation of salts in the ash cloud and/or leaching of hydrothermally deposited sulfate minerals. High concentrations of SO_4 (~1,100- to 1,700-mg/L H_2O) for leachates of all 2015 samples collected at or near the crater rim are double of the maximum reported by Witham et al. (2005) and likely represent saturation of gypsum and other sulfates during the leaching procedure. Macroscopic sulfate particles are observed in some ash samples, and XRD analysis of the May 2011 samples confirmed the presence of gypsum, anhydrite, and/or bassanite (Geirsson et al., 2014). Transition and heavy metal concentrations in ash leachates are moderately variable between the 2011 and 2015 eruptions, with significantly higher concentrations in leachates of an ash sample collected at the crater rim during the May eruptions.

XRD analysis was conducted on ash samples at Penn State using a PANalytical Empyrean diffractometer. XRD peaks identified indicate the presence of hydrothermal minerals including gypsum, anhydrite, halite, and hematite. The primary igneous phases are plagioclase feldspar and clinopyroxene (Table 5).

3.5.2. Modal Analysis

Modal analysis of three ash samples (one collected on the crater rim the day before the 22 November eruption and two collected at different distances from the vent a few hours after the 22 November eruption) was conducted to investigate the mineralogy and nature of eruptive products. The ash samples were prepared by sieving to keep the >250-μm fraction, followed by cleaning with water and an ultrasound bath. The samples

Table 5

Ash Mineralogy by X-ray Diffraction

Sample	Plagioclase	Clinopyroxene	Hematite	Magnetite	Gypsum	Anhydrite	Bassanite
TEL160511	x	x	x		x	x	X
TEL180511	x	x	x	x	x		x
TEL210511	x	x	x		x	x	
TEL210515	x	x	x		x	x	
TEL220515a	x	x	x		x	x	
TEL220515b	x	x	x		x	x	

Note. Although magnetite was only detected by X-ray Diffraction in one sample, trace Fe-Ti oxides were visually detected in several samples.

were then dried at 60 °C, then resieved to keep the 250- to 500-μm fraction. Following Suzuki et al. (2013), we made observations under a microscope to define the following families of fragments: (1) fresh: glassy, well-preserved fragments (e.g., Alvarado et al., 2016); (2) partly altered: metallic luster, second mineralization; (3) strongly altered: milky-whitish hydrothermal fragments, pyrite; and/or (4) free crystals: green transparent, translucent. Point counting between 1,025 and 1,134 fragments per sample was used to obtain a representative proportion of each family (Table 3). Point counting indicates 4.7% to 10.7% fresh glassy material in the sieved portion of the samples.

4. Discussion

Key aspects of the 2015 eruption are (1) a series of strong vulcanian explosions occurring in three discrete phases over a period of approximately 6 months, (2) eruption of hydrothermally altered basaltic-andesite and hydrothermal minerals throughout the eruptive episode and a small component of juvenile, unaltered ash during Phase 2 and Phase 3, (3) syneruptive inflation detected by cGPS and InSAR beginning with the onset of Phase 1 and continuing through the eruption period, (4) extremely low rates of LF seismicity and swarms of HF seismicity prior to and through the eruption period, followed by a return to moderate and relatively steady rates of seismicity following the eruption, (5) moderate SO_2 emissions during restless but noneruptive periods in 2013 and 2016, contrasting with negligible SO_2 emissions immediately before the 22 November explosion and high SO_2 emissions immediately following the 22 November explosion, and (6) a possible, though poorly characterized, decrease in temperature prior to the eruption onset.

Here, we compare observations during the 2015 eruption to prior observations of eruptive activity at Telica, assess evidence for a new input of magma into Telica's shallow plumbing system in 2015 and for the existence of a vertically extensive column of convecting magma in the conduit, build on previous work to develop a generalized model for persistently restless volcanism, and assess the forecasting implications of this model.

4.1. Comparison of 2015 Activity to 2011 Activity at Telica

Overall, some characteristics of Telica's 2015 eruption are similar to those observed prior to and during the 2011 eruption. However, there also exist key differences. First, the 2015 eruption was protracted, occurring in three discrete phases over a period of 5 months, compared to the single monthlong phase of the 2011 eruption. Second, ballistic blocks were larger and were deposited further from the vent in 2015 than in 2011 and eruptive columns reached greater heights. Both the 2011 and 2015 eruptions were preceded by a monthlong decline in seismicity rates (Figures 3 and 5). Similar to the 2011 eruption (Roman et al., 2016), seismicity rates were low prior to individual explosions. However, a swarm of HF events immediately preceded the April, September, and November phase onsets in 2015, and seismicity rates remained low through the end of each phase, while LF seismicity rates increased sharply toward the end of the 2011 phase. Following both the 2011 and 2015 eruptions, rates of LF seismicity reached sustained high levels. Syneruptive deformation was observed in 2015 but not in 2011. Precursory temperature drops were observed prior to both the 2011 and 2015 eruptions (through the 2015 temperature drop is based on a single measurement), and temperatures returned to high levels immediately following explosions. Gas emission data are unavailable prior to the May and September 2015 eruption phases; however, prior to the November phase gas emissions were negligible, as also observed prior the 2011 eruption onset. Following the May and November explosions, gas emissions were high, as also observed immediately following the 2011 eruption. Overall, the higher explosion energy, precursory HF swarms, syneruptive deformation, and high gas emissions following the 22 November explosion suggest higher pressures in Telica's shallow plumbing system immediately before and through the 2015 eruption as compared to the 2011 eruption. This raises the question of whether more efficient sealing of the system (see section 4.4) or a sluggish upward rise of magma into the shallow plumbing system in 2015 was responsible for increased shallow pressure.

4.2. Was the 2015 Eruption Phreatic or Phreatomagmatic?

Based on the absence of juvenile, nonhydrothermally altered shards in eruptive products, of observable deformation, and of deep seismicity, Geirsson et al. (2014) argued that Telica's 2011 eruption was phreatic. In contrast, we find evidence to suggest that the 2015 eruption, or at least its later phases, involved mobilization of magma in the shallow volcanic system. Deflation observed with cGPS and InSAR suggest

depressurization following the onset of Phase 1, and the presence of juvenile, unaltered material in the September and November phase eruptive products (Table 3) suggests that at least some juvenile magma was erupted in late 2015. High SO_4 concentrations relative to those in Taylor & Stoiber, 1973 (Table 4), in contrast, are indicative of fragmenting and erupting of the hydrothermal system in Phase 1. Although we are unable to locate earthquakes due to degradation of the seismic network by 2015, the occurrence of HF swarms preceding each eruption phase in 2015 is consistent with observations preceding other magmatic and phreatomagmatic eruptions (e.g., de Moor et al., 2019; Roman et al., 2008; Salvage et al., 2018) and indicative of increased pressurization of the plumbing system. Together, these observations suggest mobilization of magma within Telica's conduit in 2015.

4.3. Convecting Magma Column or Second Boiling of a Stagnant Shallow Magma Body

Two viable mechanisms to explain the persistence of unrest over decades at PRVs are (a) degassing-induced conduit convection (e.g., Fowler & Robinson, 2018; Kazahaya et al., 1994) and (b) crystallization-induced vapor saturation ("second boiling") of a stagnant magma body (e.g., Fowler & Spera, 2008; Stock et al., 2016). The following arguments lead us to favor a vertically extensive convecting magma column over a stagnant shallow magma body as the source of long-term unrest at Telica: First, second boiling is generally invoked at volcanoes known to be underlain by large magma chambers (e.g., Campi Flegrei, Stock et al., 2016; Yellowstone; Fowler & Spera, 2008; Cassidy et al., 2019), with the implication that pressures generated by second boiling of small volumes of magma are insufficient for eruption triggering. There is no evidence of a large magma chamber beneath Telica, as indicated by the absence of thermal and/or degassing anomalies outside the active vent and by its relatively low long-term extrusion rate (Carr et al., 2007). Finally, textural evidence in the form of sieve textures and crystal size distributions in erupted plagioclase phenocrysts implies complex mixing and pressure histories (Witter et al., 2016).

4.4. Towards a Generalized Model for Persistently Restless Volcanism

There is evidence that sealing of the shallow system played a role in the 2015 eruption, as indicated by precursory declines in seismicity and crater floor temperature preceding Phase 1 and in SO_2 degassing prior to Phase 3, and the bulk of the erupted ash was nonjuvenile and hydrothermally altered material. Sealing may be driven by mineral precipitation (e.g., Barberi et al., 1992 and references therein) or increased overburden from inner crater landslides (e.g., Hanagan & la Femina, 2017) during some episodes (e.g., 2011) and by degassing-induced crystallization of fresh magma (i.e., formation of a shallow magma plug at the top of the conduit) in other episodes. We note that the latter mechanism has been invoked to explain short-term decreases in degassing prior to explosive magmatic eruptions (e.g., Daag et al., 1996; de Moor et al., 2019; Fischer et al., 1994; Fischer et al., 2002; Kazahaya et al., 2016; Yokoo et al., 2013), though it is unclear that this mechanism played a significant role in the 2015 eruption. Alternatively, there is evidence that persistent passive degassing may also trigger eruptions by inducing the opening of magma pathways (Girona et al., 2015).

Based on the models of Geirsson et al. (2014) and Rodgers et al. (2015) and our multiparameter observations at Telica over a 7-year period, we propose that three distinct states of conduit convection occur at Telica over decadal timescales (Figure 13), all of which appear to have been observed during the TESAND deployment: (1) A stable open state (2000 to early 2010; mid-2016 onward) in which steady conduit convection leads to stable rates of LF (high rates) and HF (low rates) seismicity with moderate gas emissions and occasional small and isolated (VEI 0) explosions. Two unstable states may lead to eruptions: (2) A sealed state (1999 and 2011 eruptions and Phase 1 of 2015) in which weak sealing above the top of a convecting column of magma by chemical precipitation and/or accumulated overburden leads to gradual declines in LF seismicity, degassing, and temperature and a series of weak/phreatic explosions resulting from underlying steady in-conduit convection and/or steady-state degassing. If an eruption phase is able to fully break the seal, as it did in May 2011, the system immediately returns to the stable open state. 3. If the seal is not fully opened, a destabilized state (Phases 2 and 3 of the 2015 eruption; perhaps the 1982 eruption, which was characterized by strong explosions and ash columns to 4 km) arises in response to enhanced in-conduit convection and rapid pressure accumulation in the shallow system, producing deformation, HF swarms, and strong/impulsive phreatomagmatic explosions. Either new magma intrusion or a "failed" seal-breaking eruption could lead to destabilization of the convecting magma—based on the timing and magnitude of deformation, and the formation of a new vent during Phase 1, we suggest that the latter mechanism led to
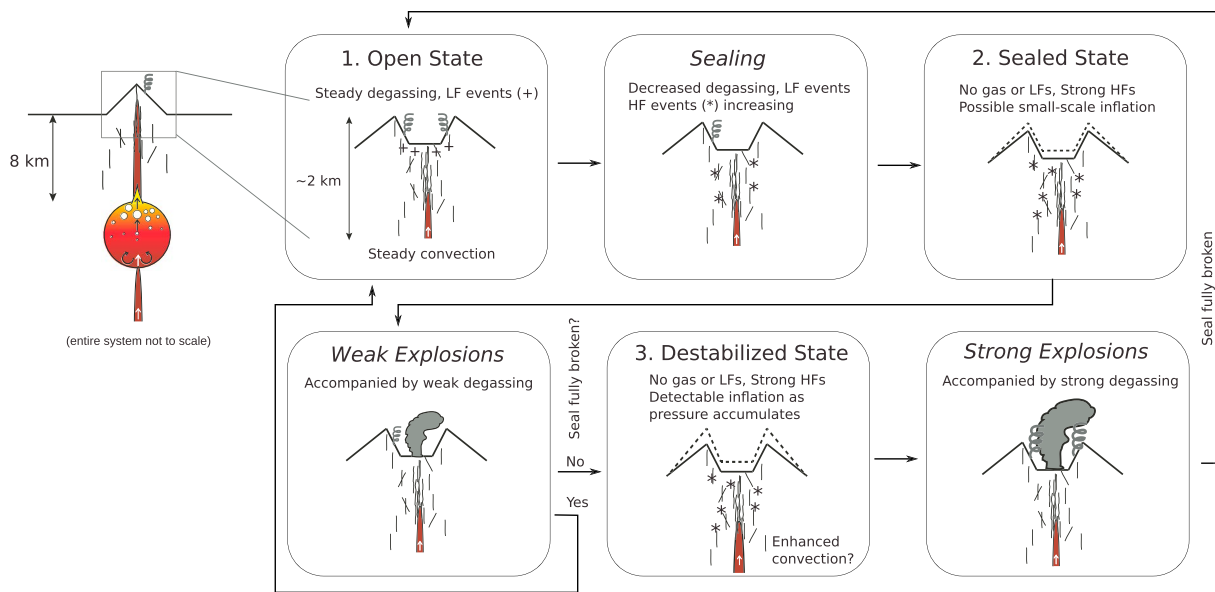
Figure 13. Conceptual model of "stable" and "unstable" states and transitional behavior at Telica and similar persistently restless volcanoes over multidecadal timescales. Telica cycles from an open state through a sealed state leading to weak explosions. If the weak explosions are able to fully break the seal and relieve accumulated pressure, the stable open state is reattained, as in 2011. If the weak explosions are unable to fully relieve accumulated pressure, the shallow magmatic system is destabilized, leading to rapid accumulation of pressure that leads to strong explosions, as in 2015. The system then returns to a stable open state. See text for details. HF = high frequency; LF = low frequency.

destabilization in 2015. Following destabilization during Phase 1, stronger explosions occurred until the seal was ultimately broken (perhaps reflected by the high post-22 November SO_2 release) and the system returned to a stable open state in December 2015.

4.5. Forecasting Implications

An idealized model for volcanic unrest involves a relatively rapid (days-months) transition from quiescence to eruption with a short-lived unrest phase in between (Sparks, 2003). This paradigm is not relevant to volcanoes characterized as PRVs; thus, forecasts of impending activity must be based on alternate models. In contrast to "typical" precursory sequences, a decrease in LF seismicity rates occasionally accompanied or followed by an increase in HF seismicity rates (consistent with a transition from open- to closed-system behavior) appears to have been prognostic of eruption likelihood at Telica: Such a pattern has now been documented prior to the 1999 (Rodgers et al., 2015), 2011 (Geirsson et al., 2014Rodgers et al., 2015), and 2015 eruptions. Decreases in gas emissions and/or crater floor temperature preceding eruptions have also been documented for the 2011 and 2015 events and may thus also be indicators of short-term eruption likelihood. Deformation may indicate the potential for more energetic and/or prolonged eruptive activity. Similarly, low seismicity rates following explosions may indicate the potential for additional phases of unrest (e.g., eruption duration). These indicators suggest that continuous seismic, deformation, gas emission, and thermal monitoring and interpretation of these data within a paradigm of sustained in-conduit convection modulated by episodes of sealing and input of fresh magma may allow robust forecasting of eruption likelihood, energy, and duration at Telica and perhaps also at similar PRVs worldwide. Future work to compare Telica's recent pattern of precursory unrest to well-documented precursory patterns at other PRVs is thus a critical next step in understanding the mechanisms of and precursors to PRV eruptions.

5. Conclusions

PRVs appear to experience multiple distinct states of unrest that reflect a combination of (a) sustained/stable noneruptive in-conduit convection, (b) series of weak explosions that unseal the shallow conduit and promote a return to stable in-conduit convection, and (c) explosions that fail to fully open the system, leading to unstable in-conduit convection and strong explosions. Over decadal timescales PRVs may exhibit all of

these distinct states of unrest, only two of which correspond to a high probability of eruption. Assessment of the state of a PRV and forecasting of the likelihood and energy of eruptive activity may be accomplished through long-term monitoring and joint interpretation of key parameters such as seismicity, deformation, degassing, and surficial temperatures. The depth of the convecting magma column and the processes that lead to periods of enhanced convection remain unclear. However, deeper processes within the convecting column may ultimately be key to sustaining restlessness over decades or longer. Overall, evidence for multiple states of unrest over a 7-year period of consistent observations at Telica highlights the need for additional long-term multiparameter studies of low-extrusion rate PRVs.

References

Altamimi, Z., Collilieux, X., & Métivier, L. (2011). ITRF2008: An improved solution of the international terrestrial reference frame. *Journal of Geodesy*, *85*(8), 457–473. https://doi.org/10.1007/s00190-011-0444-4

Alvarado, G. E., Mele, D., Dellino, P., de Moor, J. M., & Avard, G. (2016). Are the ashes from the latest eruptions (2010-2016) at Turrialba volcano (Costa Rica) related to phreatic or phreatomagmatic events? *Journal of Volcanology and Geothermal Research*, *327*, 407–415. https://doi.org/10.1016/j.jvolgeores.2016.09.003

Andres, R. J., & Kasgnoc, A. D. (1998). A time-averaged inventory of subaerial volcanic sulfur emissions. *Journal of Geophysical Research*, *103*(D19), 25,251–25,261. https://doi.org/10.1029/98JD02091

Berardino, P., Fornaro, G., Lanari, R., & Sansosti, E. (2002). A new algorithm for surface deformation monitoring based on small baseline differential SAR interferograms. *IEEE Geoscience and Remote Sensing*, *40*(11), 2375–2383. https://doi.org/10.1109/TGRS.2002.803792

Barberi, F., Bertagnini, A., Landi, P., & Principe, C. (1992). A review on phreatic eruptions and their precursors. *Journal of Volcanology and Geothermal Research*, *52*(4), 231–246.

Carr, M. J., Saginor, I., Alvarado, G. E., Bolge, L. L., Lindsay, F. N., Milidakis, K., et al. (2007). Element fluxes from the volcanic front of Nicaragua and Costa Rica. *Geochemistry, Geophysics, Geosystems*, *8*, Q06001. https://doi.org/10.1029/2006GC001396

Cashman, K. V., Sparks, R. S. J., & Blundy, J. D. (2017). Vertically extensive and unstable magmatic systems: A unified view of igneous processes. *Science*, *355*(6331), eaag3055. https://doi.org/10.1126/science.aag3055

Cassidy, M., Ebmeier, S., Helo, C., Watt, S., Caudron, C., Castro, J., 2019. Explosive eruptions with little warning: Experimental petrology and geodetic observations from the 2014 eruption of Kelud, Indonesia. EGU General Assembly.

Conde, V., Nilsson, D., Galle, B., Cartagena, R., & Muñoz, A. (2014). A rapid deployment instrument network for temporarily monitoring volcanic SO_2 emissions—A case study from Telica volcano. *Geoscientific Instrumentation, Methods and Data Systems*, *3*(2), 127–134. https://doi.org/10.5194/gi-3-127-2014

Conde, V., Robidoux, P., Avard, G., Galle, B., Aiuppa, A., Muñoz, A., & Giudice, G. (2014). Measurements of volcanic SO_2 and CO_2 fluxes by combined DOAS, Multi-GAS and FTIR observations: A case study from Turrialba and Telica volcanoes. *International Journal of Earth Sciences*, *103*(8), 2335–2347. https://doi.org/10.1007/s00531-014-1040-7

Daag, A. S., Tubianosa, B. S., Newhall, C. G., Tungol, N. M., Javier, D., Dolan, M. T., et al. (1996). Monitoring sulfur dioxide emission at Mount Pinatubo. In C. G. Newhall & R. S. Punongbayan (Eds.), *Fire and mud: Eruptions and lahars of Mount Pinatubo, Philippines* (pp. 409–414). Washington DC: University of Washington Press.

de Moor, J. M., Kern, C., Avard, G., Muller, C., Aiuppa, A., Saballos, A., et al. (2017). A new sulfur and carbon degassing inventory for the Southern Central American Volcanic Arc: The importance of accurate time-series data sets and possible tectonic processes responsible for temporal variations in arc-scale volatile emissions. *Geochemistry, Geophysics, Geosystems*, *18*, 4437–4468. https://doi.org/10.1002/2017GC007141

de Moor, J. M., Stix, J., Avard, G., Muller, C., Corrales, E., Diaz, J. A., & Alan, A. (2019). Insights on hydrothermal-magmatic interactions and eruptive processes at Poás Volcano (Costa Rica) from high-frequency gas monitoring and drone measurements. *Geophysical Research Letters*, *46*, 1293–1302. https://doi.org/10.1029/2018GL080301

Ebmeier, S. K., Biggs, J., Mather, T. A., & Amelung, F. (2013). On the lack of InSAR observations of magmatic deformation at Central American volcanoes. *Journal of Geophysical Research: Solid Earth*, *118*, 2571–2585. https://doi.org/10.1002/jgrb.50195

Fischer, T. P., Morrissey, M. M., Calvache, V. M. L., Gomez, M. D., Torres, C. R., Stix, J., & Williams, S. N. (1994). Correlations between SO_2 flux and long-period seismicity at Galeras volcano. *Nature*, *368*(6467), 135–137. https://doi.org/10.1038/368135a0

Fischer, T. P., Roggensack, K., & Kyle, P. R. (2002). Open and almost shut case for explosive eruptions: Vent processes determined by SO_2 emission rates at Karymsky volcano, Kamchatka. *Geology*, *30*(12), 1059–1062. https://doi.org/10.1130/0091-7613(2002)030<1059:OAASCF>2.0.CO;2

Fowler, A. C., & Robinson, M. (2018). Counter-current convection in a volcanic conduit. *Journal of Volcanology and Geothermal Research*, *356*, 141–162. https://doi.org/10.1016/j.jvolgeores.2018.03.004

Fowler, S. J., & Spera, F. J. (2008). Phase equilibria trigger for explosive volcanic eruptions. *Geophysical Research Letters*, *35*, L08309. https://doi.org/10.1029/2008GL033665

Galle, B., Johansson, M., Rivera, C., Zhang, Y., Kihlman, M., Kern, C., et al. (2010). Network for Observation of Volcanic and Atmospheric Change (NOVAC)—A global network for volcanic gas monitoring: Network layout and instrument description. *Journal of Geophysical Research*, *115*, D05304. https://doi.org/10.1029/2009JD011823

Geirsson, H., Rodgers, M., LaFemina, P., Witter, M., Roman, D. C., Muñoz, A., et al. (2014). Multidisciplinary observations in the 2011 explosive eruption of Telica volcano, Nicaragua: Implications for the dynamics of low-explosivity ash eruptions. *Journal of Volcanology and Geothermal Research*, *271*, 55–69. https://doi.org/10.1016/j.jvolgeores.2013.11.009

Girona, T., Costa, F., & Schubert, G. (2015). Degassing during quiescence as a trigger of magma ascent and volcanic eruptions. *Scientific Reports*, *5*(1), 18212. https://doi.org/10.1038/srep18212

Global Volcanism Program (1982). Report on Telica (Nicaragua). In L. McClelland (Ed.), *Scientific Event Alert Network Bulletin*, *Smithsonian Institution* (Vol. 7). https://doi.org/10.5479/si.GVP.SEAN198202-344040

Global Volcanism Program (1996). Report on Telica (Nicaragua). In R. Wunderman (Ed.), *Bulletin of the Global Volcanism Network, 21:4*, *Smithsonian Institution* (Vol. 21). https://doi.org/10.5479/si.GVP.BGVN199604-344040

Global Volcanism Program (2000). Report on Telica (Nicaragua). In R. Wunderman (Ed.), *Bulletin of the Global Volcanism Network*. Smithsonian Institution (Vol. 25). https://doi.org/10.5479/si.GVP.BGVN200002-344040

Global Volcanism Program (2011). Report on Telica (Nicaragua). In R. Wunderman (Ed.), *Bulletin of the Global Volcanism Network*, *Smithsonian Institution* (Vol. 36). https://doi.org/10.5479/si.GVP.BGVN201111-344040

Global Volcanism Program (2018). Report on Telica (Nicaragua). In E. Venzke (Ed.), *Bulletin of the Global Volcanism Network*, *Smithsonian Institution* (Vol. 43). https://doi.org/10.5479/si.GVP.BGVN201809-344040

Hanagan, C., la Femina, P.C., 2017. Photogrammetric analysis of changes in crater morphology at Telica Volcano, Nicaragua from 1994 to 2016. Abstract presented at 2017 AGU Fall Meeting, New Orleans, LA, 11-15 Dec.

Haney, M. M., Power, J., West, M., & Michaels, P. (2012). Causal instrument corrections for short-period and broadband seismometers. *Seismological Research Letters*, *83*(5), 834–845. https://doi.org/10.1785/0220120031

Hanssen, R. F. (2001). *Radar interferometry: Data interpretation and error analysis* (Vol. 2). New York: Springer Science & Business Media. https://doi.org/10.1007/0-306-47633-9

Johnson, J. B., & Aster, R. C. (2005). Relative partitioning of acoustic and seismic energy during Strombolian eruptions. *Journal of Volcanology and Geothermal Research*, *148*(3-4), 334–354. https://doi.org/10.1016/j.jvolgeores.2005.05.002

Johnson, J. H., Prejean, S., Savage, M. K., & Townend, J. (2010). Anisotropy, repeating earthquakes, and seismicity associated with the 2008 eruption of Okmok volcano, Alaska. *Journal of Geophysical Research*, *115*, B00B04. https://doi.org/10.1029/2009JB006991

Kazahaya, K., Shinohara, H., & Saito, G. (1994). Excessive degassing of Izu-Oshima volcano: magma convection in a conduit. *Bulletin of Volcanology*, *56*(3), 207–216. https://doi.org/10.1007/BF00279605

Kazahaya, R., Shinohara, H., Mori, T., Iguchi, M., & Yokoo, A. (2016). Pre-eruptive inflation caused by gas accumulation: Insight from detailed gas flux variation at Sakurajima volcano, Japan. *Geophysical Research Letters*, *43*, 11–219. https://doi.org/10.1002/2016GL070727

Kumagai, H., Lacson, R., Maeda, Y., Figueroa, M. S., & Yamashina, T. (2014). Shallow S wave attenuation and actively degassing magma beneath Taal Volcano, Philippines. *Geophysical Research Letters*, *41*, 6681–6688. https://doi.org/10.1002/2014GL061193

LaFemina, P.C., 1997. Monitoring soil mercury and soil gas radon and carbon dioxide at two active volcanoes: Cerro Negro and Telica, Nicaragua. M.Sc. thesis, Florida International University, Miami, USA.

Locke, C. A., Rymer, H., & Cassidy, J. (2003). Magma transfer processes at persistently active volcanoes: Insights from gravity observations. *Journal of Volcanology and Geothermal Research*, *127*(1-2), 73–86. https://doi.org/10.1016/S0377-0273(03)00179-3

Lundgren, P., Usai, S., Sansosti, E., Lanari, R., Tesauro, M., Fornaro, G., & Berardino, P. (2001). Modeling surface deformation observed with SAR interferometry at Campi Flegrei Caldera. *Journal of Geophysical Research*, *106*, 19–19.

Massonnet, D., & Feigl, K. L. (1995). Discrimination of geophysical phenomena in satellite radar interferograms. *Geophysical Research Letters*, *22*(12), 1537–1540. https://doi.org/10.1029/95GL00711

Mather, T. A., Pyle, D. M., Tsanev, V. I., McGonigle, A. J. S., Oppenheimer, C., & Allen, A. G. (2006). A reassessment of current volcanic emissions from the Central American arc with specific examples from Nicaragua. *Journal of Volcanology and Geothermal Research*, *149*(3-4), 297–311. https://doi.org/10.1016/j.jvolgeores.2005.07.021

Mori, J. J., White, R. A., Harlow, D. H., Okubo, P. G., Power, J. A., Hoblitt, R. P., et al. (1996). Volcanic earthquakes following the 1991 climactic eruption of Mount Pinatubo; Strong seismicity during a waning eruption. In C. G. Newhall & R. S. Punongbayan (Eds.), *Fire and Mud: Eruptions and Lahars of Mount Pinatubo* (pp. 339–350). Washington DC: Philippines. University of Washington Press.

Nakada, S., Shimizu, H., & Ohta, K. (1999). Overview of the 1990–1995 eruption at Unzen Volcano. *Journal of Volcanology and Geothermal Research*, *89*(1-4), 1–22. https://doi.org/10.1016/S0377-0273(98)00118-8

Park, I., Jolly, A., Kim, K. Y., & Kennedy, B. (2019). Temporal variations of repeating low frequency volcanic earthquakes at Ngauruhoe Volcano, New Zealand. *Journal of Volcanology and Geothermal Research*, *373*, 108–119. https://doi.org/10.1016/j.jvolgeores.2019.01.024

Petersen, T., Caplan-Auerbach, J., & McNutt, S. R. (2006). Sustained long-period seismicity at Shishaldin Volcano, Alaska. *Journal of Volcanology and Geothermal Research*, *151*(4), 365–381. https://doi.org/10.1016/j.jvolgeores.2005.09.003

Powell, T.W., 2004. Characterisation of volcano-seismic events and their relation to volcanic processes in the Montserrat eruption. Ph.D. Dissertation, University of Leeds, Leeds, UK.

Power, J. A., Stihler, S. D., Chouet, B. A., Haney, M. M., & Ketner, D. M. (2013). Seismic observations of Redoubt Volcano, Alaska—1989–2010 and a conceptual model of the Redoubt magmatic system. *Journal of Volcanology and Geothermal Research*, *259*, 31–44. https://doi.org/10.1016/j.jvolgeores.2012.09.014

Reath, K., Pritchard, M., Poland, M., Delgado, F., Carn, S., Coppola, D., et al. (2019). Thermal, deformation, and degassing remote sensing time series (CE 2000–2017) at the 47 most active volcanoes in Latin America: Implications for volcanic systems. *Journal of Geophysical Research: Solid Earth*, *124*, 195–218. https://doi.org/10.1029/2018JB016199

Rizzoli, P., Martone, M., Gonzalez, C., Wecklich, C., Borla Tridon, D., Bräutigam, B., et al. (2017). Generation and performance assessment of the global TanDEM-X digital elevation model. *ISPRS Journal of Photogrammetry and Remote Sensing*, *132*, 119–139. https://doi.org/10.1016/j.isprsjprs.2017.08.008

Robidoux, P., Rotolo, S. G., Aiuppa, A., Lanzo, G., & Hauri, E. H. (2017). Geochemistry and volatile content of magmas feeding explosive eruptions at Telica volcano (Nicaragua). *Journal of Volcanology and Geothermal Research*, *341*, 131–148. https://doi.org/10.1016/j.jvolgeores.2017.05.007

Rodgers, M., Roman, D. C., Geirsson, H., LaFemina, P., McNutt, S. R., Muñoz, A., & Tenorio, V. (2015). Stable and unstable phases of elevated seismic activity at the persistently restless Telica Volcano, Nicaragua. *Journal of Volcanology and Geothermal Research*, *290*, 63–74. https://doi.org/10.1016/j.jvolgeores.2014.11.012

Rodgers, M., Roman, D. C., Geirsson, H., LaFemina, P. C., Muñoz, A., Guzman, C., & Tenorio, V. (2013). Seismicity accompanying the 1999 eruptive episode at Telica Volcano, Nicaragua. *Journal of Volcanology and Geothermal Research*, *265*, 39–51. https://doi.org/10.1016/j.jvolgeores.2013.08.010

Roman, D. C., De Angelis, S., Latchman, J. L., & White, R. (2008). Patterns of volcanotectonic seismicity and stress during the ongoing eruption of the Soufrière Hills Volcano, Montserrat (1995–2007). *Journal of Volcanology and Geothermal Research*, *173*(3-4), 230–244. https://doi.org/10.1016/j.jvolgeores.2008.01.014

Roman, D. C., Rodgers, M., Geirsson, H., LaFemina, P. C., & Tenorio, V. (2016). Assessing the likelihood and magnitude of volcanic explosions based on seismic quiescence. *Earth and Planetary Science Letters*, *450*, 20–28. https://doi.org/10.1016/j.epsl.2016.06.020

Saballos et al., (n.d.) [dataset] doi:10.196/novac.telica.001.

Sadofsky, S. J., Portnyagin, M., Hoernle, K., & van den Bogaard, P. (2008). Subduction cycling of volatiles and trace elements through the Central American volcanic arc: Evidence from melt inclusions. *Contributions to Mineralogy and Petrology*, *155*(4), 433–456. https://doi.org/10.1007/s00410-007-0251-3

Salvage, R. O., Avard, G., De Moor, J. M., Pacheco, J. F., Brenes Marin, J., Cascante, M., & Martínez Cruz, M. (2018). Renewed explosive phreatomagmatic activity at Poás volcano, Costa Rica in April 2017. *Frontiers in Earth Science*, *6*, 160. https://doi.org/10.3389/feart.2018.00160

Simons, M., & Rosen, P. A. (2015). *Treatise on Geophysics*. Amsterdam: Elsevier.

Sparks, R. S. J. (2003). Forecasting volcanic eruptions. *Earth and Planetary Science Letters*, *210*(1-2), 1–15. https://doi.org/10.1016/S0012-821X(03)00124-9

Stix, J. (2018). Understanding unrest at fast and slow volcanoes and implications for eruption forecasting. *Frontiers in Earth Science*, *6*, 56. https://doi.org/10.3389/feart.2018.00056

Stock, M. J., Humphreys, M. C., Smith, V. C., Isaia, R., & Pyle, D. M. (2016). Late-stage volatile saturation as a potential trigger for explosive volcanic eruptions. *Nature Geoscience*, *9*(3), 249–254. https://doi.org/10.1038/ngeo2639

Suzuki, Y., Nagai, M., Maeno, F., Yasuda, A., Hokanishi, N., Shimano, T., et al. (2013). Precursory activity and evolution of the 2011 eruption of Shinmoe-dake in Kirishima volcano-insights from ash samples. *Earth Planets Space*, *65*(6), 591–607. https://doi.org/10.5047/eps.2013.02.004

Taisne, B., Brenguier, F., Shapiro, N. M., & Ferrazzini, V. (2011). Imaging the dynamics of magma propagation using radiated seismic intensity. *Geophysical Research Letters*, *38*, L04304. https://doi.org/10.1029/2010GL046068

Taylor, P. S., & Stoiber, R. E. (1973). Soluble material on ash from active Central American volcanoes. *Geological Society of America Bulletin*, *84*(3), 1031–1042. https://doi.org/10.1130/0016-7606(1973)84<1031:SMOAFA>2.0.CO;2

Werner, C., Wegmüller, U., Strozzi, T., Wiesmann, A., 2000. Gamma SAR and interferometric processing software. Proceedings of the ERS-ENVISAT Symposium, Gothenburg, Sweden.

Wessel, B., Huber, M., Wohlfart, C., Marschalk, U., Kosmann, D., & Roth, A. (2018). Accuracy Assessment of the Global TanDEM-X Digital Elevation Model with GPS Data. *ISPRS Journal of Photogrammetry and Remote Sensing.*, *139*, 171–182. https://doi.org/10.1016/j.isprsjprs.2018.02.017

Witham, C. S., Oppenheimer, C. O., & Horwell, C. J. (2005). Volcanic ash-leachates: A review and recommendations for sampling methods. *Journal of Volcanology and Geothermal Research*, *141*(3-4), 299–326. https://doi.org/10.1016/j.jvolgeores.2004.11.010

Witter, M., Furman, T., LaFemina, P., & Feineman, M. (2016). Understanding magmatic processes at Telica volcano, Nicaragua: Crystal size distribution and textural analysis. *American Mineralogist*, *101*(5), 1052–1060. https://doi.org/10.2138/am-2016-5379

Wolfe, E. W., & Hoblitt, R. P. (1996). Overview of the eruptions. In C. G. Newhall & R. S. Punongbayan (Eds.), *Fire and mud: Eruptions and lahars of Mount Pinatubo* (pp. 3–20). Washington DC: Philippines. University of Washington Press.

World Health Organization (2011). *Guidelines for drinking-water quality, Fourth Edition*. Geneva, Switzerland: WHO Press.

Yokoo, A., Iguchi, M., Tameguri, T., & Yamamoto, K. (2013). Processes prior to outbursts of Vulcanian eruption at Showa crater of Sakurajima volcano. *Bulletin of Volcanology Society of Japan*, *58*(1), 163–181.

Zumberge, J. F., Heflin, M. B., Jefferson, D. C., Watkins, M. M., & Webb, F. H. (1997). Precise point positioning for the efficient and robust analysis of GPS data from large networks. *Journal of Geophysical Research*, *102*(B3), 5005–5017. https://doi.org/10.1029/96JB03860